Geological Quarterly, 2023, 67: 9
DOI: http://dx.doi.org/10.7306/gq.1679

Neoproterozoic ophiolite exotic blocks in the Outer Western Carpathians, southern Poland: a record of the fast ocean-floor cooling and alterations

Aleksandra GAWĘDA[1, *], Krzysztof SZOPA[1], Anna WAŚKOWSKA[2], Jan GOLONKA[2], Tomasz KRZYKAWSKI[1] and Tetiana KALINICHENKO[3]

[1] University of Silesia, Institute of Earth Sciences, Będzińska 60, 41-200 Sosnowiec, Poland, ORCID: 0000-0001-9102-2149 [AG], 0000-0002-7588-7836 [K.S.], 0000-0001-5053-5116 [T.K]

[2] Faculty of Geology, Geophysics and Environmental Protection, AGH University of Science and Technology, Al. Mickiewicza 30, 20-059 Kraków, Poland, ORCID: 0000-0003-4090-8534 [A.W.], 0000-0001-9671-5809 [J.G.]

[3] M.P. Semenenko Institute of Mineralogy, Geochemistry and Ore Formation of the National Academy of Sciences of Ukraine, Palladina 34, Kyiv-142, Ukraine

Gawęda, A., Szopa, K., Waśkowska, A., Golonka, J., Krzykawski, T., Kalinichenko, T., 2030. Neoproterozoic ophiolite exotic blocks in the Outer Western Carpathians, southern Poland: a record of the fast ocean-floor cooling and alterations. Geological Quarterly, 67: 9, doi: 10.7306/gq.1679

Ophiolitic blocks, represented by metagabbro and serpentinite containing relict pyroxene, olivine, baddeleyite, zirconolite, Ni-pyrite and pyrrhotite, were found as exotic blocks in an olistostrome in the Magura Nappe, Outer Western Carpathians. The geochemical and isotopic features of the blocks suggest they represent mantle-derived rocks, with within-plate geochemistry signatures, modified by subduction, with lithospheric mantle input. A U-Pb apatite cooling age (614 ±3 Ma) is within age uncertainty of a published U-Pb zircon magmatic crystallization age (~614 Ma) implying rapid post-crystallization cooling. Pervasive alteration with replacement of primary minerals by low-temperature assemblages is observed in all rock fragments and is interpreted as contemporaneous with shearing. The secondary mineral assemblages and temperature modelling allow the interpretation that the pervasive ocean-floor metamorphism is the alteration in these meta-mafic rocks. These ophiolitic fragments can be linked to the Neoproterozoic break up of Rodinia/Pannotia.

Key words: Outer Carpathians, Neoproterozoic, ophiolite mélange, ocean floor.

INTRODUCTION

Ophiolite complexes are mainly composed of altered serpentinites, spilite basalts, gabbros and. represent remnants of ancient oceanic crust (Steinmann, 1927). Most of ocean floor metabasalts typically show ocean-floor or hydrothermal metamorphism (see Honnorez, 2003 and references therein), and are particularly common in slow-spreading ridges (see discussion and references in Rioux et al., 2015). During subduction most of oceanic crust is recycled into the mantle. The preservation of oceanic crust is possible in places which underwent obduction, where oceanic crust is thrust over the continental wedge. Such exhumed ophiolite fragments yield information on the rifting and drift history and are also important markers for mantle-crust interaction during subduction as well as interaction between magmatic and hydrothermal processes (Dewey, 1977, 2005; Sinton and Detrick, 1992).

In this paper, we present petrological data on metabasic rocks, found as “exotic” blocks in the Magura Nappe, Outer Western Carpathians. These exotic blocks, classified as metagabbro-metadiorite and se, reaching up to one metre in size, were found within Eocene olistostrome (Wieser, 1952; Cieszkowski et al., 2017). Some of the blocks contain abundant magmatic zircon (~614 Ma, with no inherited component; Gawęda et al., 2019) and apatite. New found varieties of gabbroic and serpentinized (ultramafic) exotic blocks from the same locality are here presented in addition to a discussion of the previously published data. The nature of the mineral assemblages and the secondary alterations of the primary magmatic minerals resemble those of ocean-floor metamorphism/hydrothermal metamorphism. These assemblages and their thermal history are characterised here and new U-Pb inductively coupled plasma-mass spectrometry ICP-MS apatite age data are presented. As the studied rocks are exotic with respect to the enclosing sedimentary succesion, their significance is discussed in terms of regional plate tectonic setting.

GEOLOGICAL SETTING AND SAMPLING

The Carpathian mountain belt, located in the central part of the Alpine chain of Europe, stretches across ~1300 km and is divided into the Western, Eastern and Southern Carpathians (Fig. 1A). The Western Carpathians are subdivided into the Inner Carpathians, the Central Carpathians and the Outer

* Corresponding author, e-mail: aleksandra.gaweda@us.edu.pl

Received: August 31, 2022; accepted: January 29, 2023; first published online: March 17, 2023

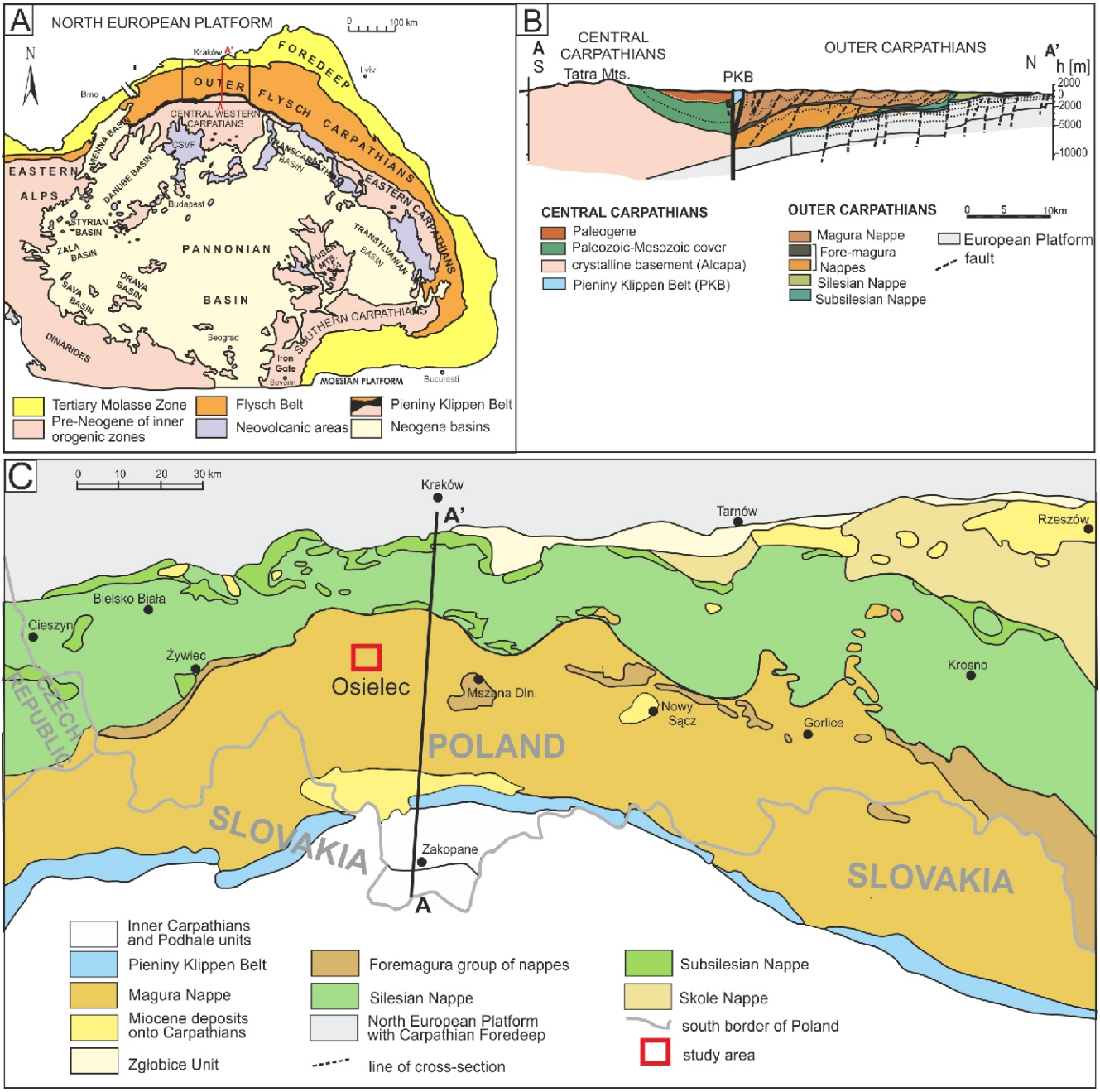

Fig. 1A – a simplified geological sketch of the Carpathian Chain (after Golonka et al., 2021, modified), B – with generalized cross-section and C – the geological map of the Outer Western Carpathians with the locations of the sampling point

Carpathians, with the last separated by the Pieniny Klippen Belt (e.g., Winkler and Ślączka, 1994; Plašienka et al., 1997; Ślączka et al., 2006; Gawęda and Golonka, 2011; Kováč et al. 2016; Golonka et al., 2021 and references therein). The Outer Western Carpathians (Fig. 1B, C) are comprised of a stack of nappes and thrust-sheets containing up to six km of Upper Jurassic–Miocene flysch sequences, which were thrust over the European Platform and autochthonous Miocene cover of the Carpathian Foredeep during the Alpine orogeny (Książkiewicz, 1977; Winkler and Ślączka, 1994; Schmid et al., 2008; Oszczypko, 2010; Kováč et al. 2016; Golonka et al., 2019 and references therein). The nappe sequences in the Outer Western Carpathians were detached from their basement (e.g., Książkiewicz, 1977; Unrug, 1968; Golonka et al., 2005; Ślączka et al., 2006) and consist, from the top to bottom of the Magura Nappe, the Fore-Magura group of nappes and the Silesian, Subsilesian and Skole nappes (Fig. 1C). The Outer Carpathian basin sedimentary rocks were thrust over the European Platform during the Alpine collision forming allochthonous nappes (Książkiewicz, 1977; Schmid et al., 2008; Oszczypko, 2010; Kováč et al. 2016; Golonka et al., 2019 and references therein).

The Western Outer Carpathian basins formed during the Mesozoic and Cenozoic in the western part of the Tethys Ocean. Their depositional basement was both the Protocarpathians, formed in the Neoproterozoic and experienced probable Variscan reworking (e.g., Poprawa et al., 2006; Budzyń et al., 2011; Burda et al., 2019; Gawęda et al., 2019, 2021; Szczuka et al., 2022) as well as the remnants of Tethyan

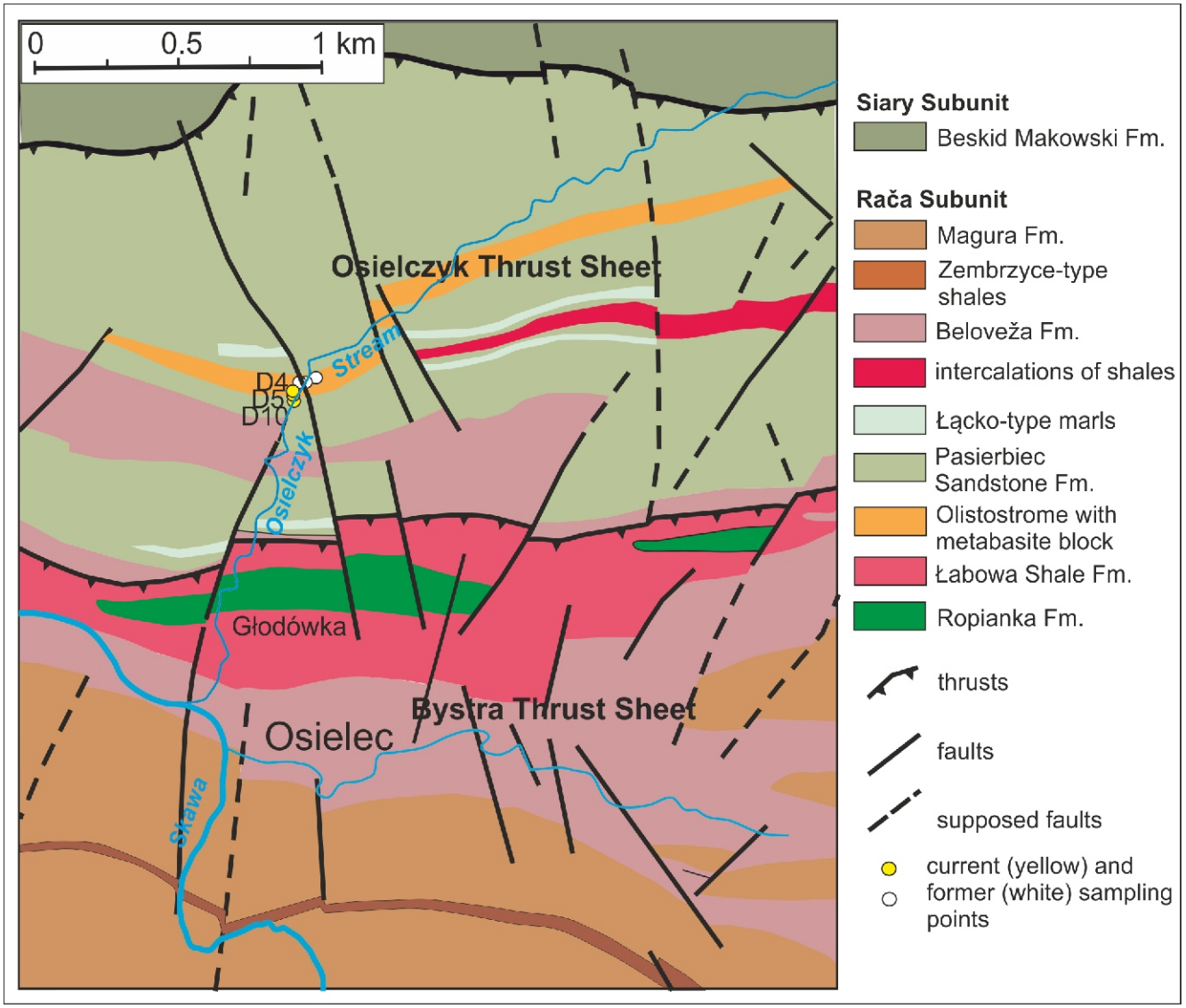

Fig. 2. Geological map of the study area (after Cieszkowski et al., 2017)

oceanic crust (Stampfli et al., 2002; Szopa et al., 2014). As the Outer Carpathian nappes are uprooted and detached from the original place of formation, the Protocarpathian basement is present as exotic blocks, which are the primary source of information on the nature and pre-Alpine history of the basement. Jurassic extension and Cretaceous to Neogene Alpine events caused the formation of sub-basins separated by basement ridges (intra-basin highs) as a result of basin inversion (Unrug 1968; Książkiewicz 1977). These ridges were a source of clastic material to the Outer Carpathian basins, with the larger clasts (i.e., the exotic blocks) transported to the inner parts of the basin where they are present within olistostromes, debrites and flysch sequences (Książkiewicz, 1975; Ślączka et al., 2006; Cieszkowski et al., 2012). Olistostromes are products of mass-wasting processes that were deposited in the submarine environment (Festa et al., 2014). They can be initiated and deposited at various depths, from shallow seas to deep oceans (Moscardelli and Wood, 2007; Ogata et al., 2012). In the outer Carpathian basins, the olistostromes are associated with deep-water flysch deposits (Książkiewicz, 1975; Ślączka et al. 2006; Cieszkowski et al., 2012). The exotic blocks are mostly found within the Silesian and Subsilesian nappes (Gawęda et al., 2019; Golonka et al., 2021). In the Magura Nappe, large blocks are occasionally found in the Krynica Zone and in the Rača Zone, and include several metagabbro- metadiorite as well as granite exotic blocks (Gawęda et al., 2019, 2021).

The clasts of mafic and ultramafic rocks (samples D4, D5, D10; Fig. 2) were collected from the Osielczyk Stream, in the southeastern part of the Osielec village in the Beskid Makowski Range (Grid reference: N49°41'09.4", E19°46'22.0"), several metres up the steam from the former sampling site (Gawęda et al., 2019). They were found within Eocene olistostrome of the Pasierbiec Member of the Beloveža Formation in the Magura Nappe (Wieser, 1952; Golonka and Waśkowska, 2012 and references therein; Cieszkowski et al., 2017). The crystalline gabbroic (D4, D5) and serpentinite (D10) clasts range from 0.3 to 2.0 m in size, are poorly rounded and located inside a sandy-conglomerate or sandy-mudstone matrix.

HISTORY OF THE RESEARCH

Blocks of mafic magmatic rocks within the Pasierbiec Sandstones of the Magura Nappe of the Outer Western Carpathians have been the subject of research for over 70 years. They were originally found by Marian Książkiewicz, during mapping in

1948. In the same year Książkiewicz invited petrographer, Tadeusz Wieser to collaborate. The material investigated was a large block of gabbro (>2 m across) in Osielczyk Stream. On the basis of petrography the rock was classified as a prasinite (a metamorphosed basalt that is a part of an ophiolite succession; Wieser, 1952). Recently, more mafic blocks were found in Osielczyk Stream (Cieszkowski et al., 2010; Kysiak, 2010) and preliminary U-Pb zircon data were presented (Anczkiewicz et al., 2016). Field work conducted in 2016–2021 was based on Marek Cieszkowski`s observations and advice, and resulted in the sampling of three smaller blocks (D4, D5 and D10 samples; Fig. 2), compared herein with previously published data (samples OSC, D3, D6, D6-2; Gawęda et al., 2019) and presented in this paper.

METHODOLOGY

MICROSCOPY

Petrographic analyses of thin sections were undertaken using an *Olympus BX-51* microscope to constrain textural and microstructural relationships and to determine the presence of apatite. The petrographical observations were used to select representative samples for subsequent electron probe micro-analysis, whole-rock geochemical and isotopic analyses, as well as apatite grain separation and subsequent U-Pb dating.

ELECTRON PROBE MICRO-ANALYSES (EPMA)

Microprobe analyses of the main rock-forming and accessory minerals were carried out using a *CAMECA SX-100* electron microprobe, at the Inter-Institutional Laboratory of Microanalyses of Minerals and Synthetic Substances, Warsaw, Poland. The analytical conditions employed an accelerating voltage of 15 kV, a beam current of 20 nA, counting times of 4 s for peak and background and a beam diameter of 1–5 mm. Reference materials, analytical lines, diffracting crystals, mean detection limits (in wt.%) and uncertainties were as follows: rutile – Ti (K , PET, 0.03, 0.05), diopside – Mg (K , TAP, 0.02, 0.11), Si – (K , TAP, 0.02, 0.21), Ca – (K , PET, 0.03, 0.16), orthoclase – Al (K , TAP, 0.02, 0.08), and K (K , PET, 0.03, 0.02), albite – Na (K , TAP, 0.01, 0.08), hematite – Fe (K , LIF, 0.09, 0.47), rhodonite – Mn (K , LIF, 0.03, 0.10), phlogophite – F (K , TAP, 0.04, 0.32), tugtupite – Cl (K , PET, 0.02, 0.04), Cr2O3 – Cr (K , PET, 0.04, 0.01), ZirconED2 – Zr (L , PET, 0.01, 0.01), Nb2O3-MAC – Nb (L , PET, 0.09, 0.01), V2O5 – V (K , LIF, 0.02, 0.01), YPO4 – Y (L , TAP, 0.05, 0.05), CeP5O14 – Ce (L , LPET, 0.09, 0.02), NdGaO3 – Nd (L , LIF, 0.31, 0.24), ThO2 – Th (M , LPET, 0.09, 0.09), UO2 – U (M , LPET, 0.16, 0.13).

WHOLE-ROCK CHEMICAL AND ISOTOPE ANALYSES

Whole-rock analyses were undertaken using X-Ray fluorescence (XRF) for major and trace large ion lithophile elements (LILE), and by fusion and ICP-MS for trace high field strength elements (HFSE) and rare earth elements (REE) at Institute of Earth Sciences, University of Silesia in Katowice (XRF) and Bureau Veritas Minerals (Canada) (ICP-MS), respectively. Preparation involved lithium borate fusion and dilute digestions for XRF and lithium borate decomposition or *aqua regia* digestion for ICP-MS. Lost on ignition (LOI) values were determined at 1000°C. Uncertainties for most of major elements are 0.01%, except for SiO_2 which is 0.1%. REE were normalized to C1 chondrite (McDonough and Sun, 1995).

The Sm-Nd and Rb-Sr analytical results were undertaken by isotope dilution-thermal ionization mass spectrometry (ID-TIMS) at the University of Vienna. Sample digestion for Nd-Sr analysis was performed in Savillex® beakers using an ultrapure 4:1 mixture of HF and HNO_3 for 10 days at 110°C on a hot plate. For whole rock powders, a minimum dissolution time of three weeks was applied to ensure maximum leaching of the REEs from refractory material such as zircon. After evaporating the acids, repeated treatment of the residue using HNO_3 and 6.0 N HCl resulted in clear solutions for all samples. The REE fraction was extracted using AG® 50W-X8 (200–400 mesh, Bio-Rad) resin and 4.0 N HCl. Nd was separated from REE using teflon-coated HdEHP, and 0.22 N HCl as the elution media. For Sr, element separation followed conventional techniques, using AG® 50W-X8 (200–400 mesh, Bio-Rad) resin and 2.5 N HCl as eluants. Maximum total procedural blanks were <1 ng for Sr and 50 pg for Nd and were taken as negligible. Nd and Sr were run as metals on a Re double filament, using a ThermoFinnigan® Triton MC TIMS. A $^{143}Nd/^{144}Nd$ ratio of 0.511841 ±0.000005 (n = 5) and a $^{87}Sr/^{86}Sr$ ratio 0.710259 ±0.000005 (n = 5) were determined for the La Jolla (Nd) and the NBS987 (Sr) international standards, respectively, during the period of investigation. Within-run mass fractionation for Nd and Sr isotope compositions (IC) was corrected to $^{146}Nd/^{144}Nd = 0.7219$ and $^{86}Sr/^{88}Sr = 0.1194$, respectively. Uncertainties on the Nd and Sr isotope ratios are quoted typically as 2 $_m$. T_{DM2stg} were calculated using the Liew and Hofmann (1988) procedure.

X-RAY DIFFRACTION

A sample of serpentinite was ground in an agate mortar until one g of powder below 20 micrometers was obtained. XRD analyzes were performed using a *PANalytical X'Pert Pro X-ray* diffractometer (PW3040/60), equipped with a cobalt anode tube (40 mA, 40 kV) and an X'Celerator detector. The analyzes were performed over a wide range of 2 (from 5 to 90°) to obtain the appropriate number of peaks for each phase, with a long counting time constant (300 s.) and a precise step size (0.02°2). The results were evaluated in the HighScore program, version 4.9 (Degen et al., 2014) linked to the ICSD (ver. 2015), COD(ver. 2021), and ICDD PDF4 + databases (ver. 2019).

MINERAL SEPARATION AND IMAGING

Apatite grains were separated from sample D5 (metagabbro) using standard density separation techniques (crushing, sieving, washing and panning). The apatite crystals were hand-picked under a binocular microscope, cast in 25 mm diameter epoxy resin mounts, and then ground and polished to expose the grain interiors. Mineral textures were then imaged using back-scattered electron (BSE) and cathodoluminescence (CL) detectors on a FET *Philips 30* scanning electron microscope with a 15 kV accelerating voltage and a beam current of 1 nA.

APATITE U-PB DATING

Apatite crystals were analyzed as separates on polished epoxy mounts. U-Pb and REE data were acquired using a laser ablation system (Photon Machines Analyte Excite 193 nm ArF Excimer) coupled to an Agilent 7900 Q-ICP MS at the Department of Geology, Trinity College Dublin. Twenty-nine isotopes

(^{31}P, ^{35}Cl, ^{43}Ca, ^{51}V, ^{55}Mn, ^{88}Sr, ^{89}Y, ^{90}Zr, ^{139}La, ^{140}Ce, ^{141}Pr, ^{146}Nd, ^{147}Sm, ^{153}Eu, ^{157}Gd, ^{159}Tb, ^{163}Dy, ^{165}Ho, ^{166}Er, ^{169}Tm, ^{172}Yb, ^{175}Lu, ^{202}Hg, ^{204}Pb, ^{206}Pb, ^{207}Pb, ^{208}Pb, ^{232}Th and ^{238}U were acquired using a 60 μm laser spot, a 11 Hz laser repetition rate and a fluence of 2.5 J/cm^2. A ~1 cm sized crystal of Madagascar apatite which has yielded a ID-TIMS concordia age of 473.5 ±0.7 Ma was used as the primary apatite reference material in this study (Cochrane et al., 2014). McClure Mountain syenite apatite (the rock from which the ^{40}Ar/^{39}Ar hornblende standard MMhb is derived) and Durango apatite were used as secondary standards. NIST 612 standard glass was used as the apatite trace-element reference material, and a crushed aliquot of Durango apatite that has been characterised by solution quadrupole-ICP-MS analyses (Chew et al., 2016), was used as the apatite trace-element secondary standard.

The raw isotope data were reduced using a modified version of the "Vizual Age" data reduction scheme (Petrus and Kamber, 2012) of the freeware IOLITE package of Paton et al. (2011). This data reduction scheme ("VizualAge_UcomPbine") can account for variable common Pb in the apatite (Chew et al., 2014). User-defined time intervals are established for the baseline correction procedure to calculate session-wide baseline-corrected values for each isotope. The time-resolved fractionation response of individual standard analyses is then characterized using a user-specified down-hole correction model (such as an exponential curve, a linear fit or a smoothed cubic spline). The data reduction scheme then fits this appropriate session-wide "model" U-Th-Pb fractionation curve to the time-resolved standard data and the unknowns. Sample-standard bracketing is applied after the correction of down-hole fractionation to account for long-term drift in isotopic or elemental ratios by normalizing all ratios to those of the U-Pb reference standards. Common Pb in the apatite standards and unknowns was corrected using a ^{207}Pb-based correction in VizualAge_UcomPbine and includes the propagation of the uncertainties in the age of the reference materials. McClure Mountain syenite apatite (total Pb/U isochron age of 525.3 ± 1.7 Ma; Krestianinov et al., 2021) and Durango apatite (linear 3-D isochron age of 32.683 ±0.050 Ma; Paul et al., 2021) were used as secondary standards and yielded weighted average ^{207}Pb-corrected ages of 527.3 ±3.1 Ma (MSWD = 1.2) and 31.71 ±0.59 Ma (MSWD = 1.7) respectively, using a ^{207}Pb/^{206}Pb value of 0.874 derived from an apatite ID-TIMS total U-Pb isochron (Krestianinov et al., 2021) and a ^{207}Pb/^{206}Pb value derived from the Stacey and Kramers (1975) terrestrial Pb evolution model at 32.68 Ma. Age calculation was done using Isoplot R software (Vermeesch, 2018). All apatite REE contents were normalized to C1 chondrite (McDonough and Sun, 1995).

RESULTS

PETROGRAPHY AND MINERAL CHEMISTRY

Three main varieties of rocks can be distinguished: (1) massive, medium-grained, metagabbro-metadiorite, with abundant accessory minerals (D5; Fig. 3A, C–G); (2) extensively altered fine-grained banded rock (prasinite; D4; Fig. 3G); (3) black foliated serpentinite (D10; Fig. 3B, H–J). The first two varieties were petrographically described by Gawęda et al. (2019) and are re-examined herein, using new samples.

Massive metagabbro-metadiorite (D5) shows pronounced secondary alterations (Fig. 3D–F). It is composed of three varieties of amphiboles, plagioclase, epidote+titanite+chlorite±calcite, that form pseudomorphs after unknown primary phases (pyroxene? Fig. 4A; see Gawęda et al., 2019) and rutile+hematite+titanite pseudomorphs after ilmenite (Fig. 4A, B).

Of the amphibole group minerals, magnesio-hornblende (Figs. 3C, D and 5), with a TiO_2 content ranging from 0.66 wt.%. to 1.58 wt.%. (Table 1) represents the late- to post-magmatic phase of crystallization, probably crystallizing at the cost of early stage minerals reacting with evolved water-rich melt (Fig. 3C, E; Costa et al., 2002 and references therein). Amphibole classification is based on the recommendations of the International Mineralogical Association (IMA) subcommittee on amphiboles (Leake et al., 1998). The calibrated temperature of crystallization (based on the calibration of Ridolfi et al. 2010) ranges from 797 to 767°C, at a pressure of 112 to 96 MPa (Table 1). Mg-hornblende is locally in textural equilibrium with plagioclase $An_{39\text{-}51}Ab_{46\text{-}57}Or_2$, rimmed by albite. Actinolitic hornblende (TiO_2 = 0.85 – 0.22 wt.%) usually form rims on magnesio-hornblende (Fig. 3D, F) while actinolite (TiO_2 = 0.31–0.01 wt.%) forms the pseudomorphs or the most external rims (Figs. 3D, G and 4C; Table 1). The calibrated temperatures of crystallization for the late-magmatic low-Ti amphiboles range from 733 to 629°C and the pressure from 68 to 30 MPa (Table 1). In the case of the very low-Ti actinolite the pressure and temperature calculations are not applicable. Biotite is a secondary phase, growing at the expense of opaque minerals, showing no late shearing textures. Epidote and titanite (Table 2) are usually intergrown, forming – together with spinels/rutile, pseudomorphs after an unknown phase (pyroxene?; Figs. 3E and 4A, D). Mn-ilmenite is sporadically found, usually replaced by Ti-hematite and rutile with Ti, Nb, Zr, V substitutions (Table 3). These two minerals, closely intergrown, form pseudomorphs, usually rimmed by titanite (Fig. 4A, B). Fluorapatite is locally abundant as idiomorphic crystals ranging from 50 to 300 mm in diameter (Fig. 3C, D). Fluorapatite contains inclusions of amphibole and plagioclase (Figs. 3C and 4G, H), while it is locally intergrown with chlorite with albite on its rims (Fig. 4H) and represent the post-magmatic crystallization. Together with titanite, apatite is the main carrier of REE. Apatite crystals are slightly zoned with respect to Mn (from 323 to 609 ppm) and REE, with REE ranging from 1844 ppm (at rims) to 5864 ppm (in cores; Appendix 1). Their chondrite(C1)-normalized REE patterns show slight LREE enrichment (Ce_N/Yb_N = 5.94 – 16.6) and strong negative Eu anomalies (Eu/Eu* = 0.27–0.54; Appendix 1). Accessory zircon forms idiomorphic crystals up to 200 mm in diameter (Gawęda et al., 2019; Fig. 4D). Pyrrhotite is partly replaced by goethite. Calcite is a secondary phase, filling fissures.

Banded prasinite rock (*sensu* Wiser, 1952; sample D4) is composed of intergrown chlorite, epidote, titanite with secondary quartz bands (Fig. 3C) locally with albite and actinolite patches, with secondary quartz bands, underwent extensive shearing (Gawęda et al., 2019). Chlorite contain 59–83% of the clinochlore $(Mg_5Al)(Si_3Al)O_{10}(OH)$ end-member, 10–38% of the chamosite $(Fe^{2+}_5Al)(Si_3Al)O_{10}(OH)$ end-member and up to 9% of the pennite $(Mn_5Al)(Si_3Al)O_{10}(OH)$ end-member (classification after Bailey, 1980; Table 4; analyses #1–#5), while epidote and titanite share the same range of chemical compositions as the massive gabbro-diorite (Table 2). No magmatic mineral assemblages are preserved, except accessory apatite and zircon (up to 100 mm in diameter).

Serpentinite (sample D10) is formed mainly by antigorite (Fig. 6), with small amount of lizardite (~6 vol%), with sporadic remnants of Mg-rich olivine ($Fo_{88}Fa_{12}$; Table 5 and Fig. 3I) and weakly zoned pyroxene (Al-Cr-diopside to diopside; Table 5 and Fig. 3H). Locally, ghost-structures of albitic pseudomorphs after primary plagioclases are present (Fig. 3J). Chlorite (Table 4; analyses #6–#10) and calcite are seen filling fissures.

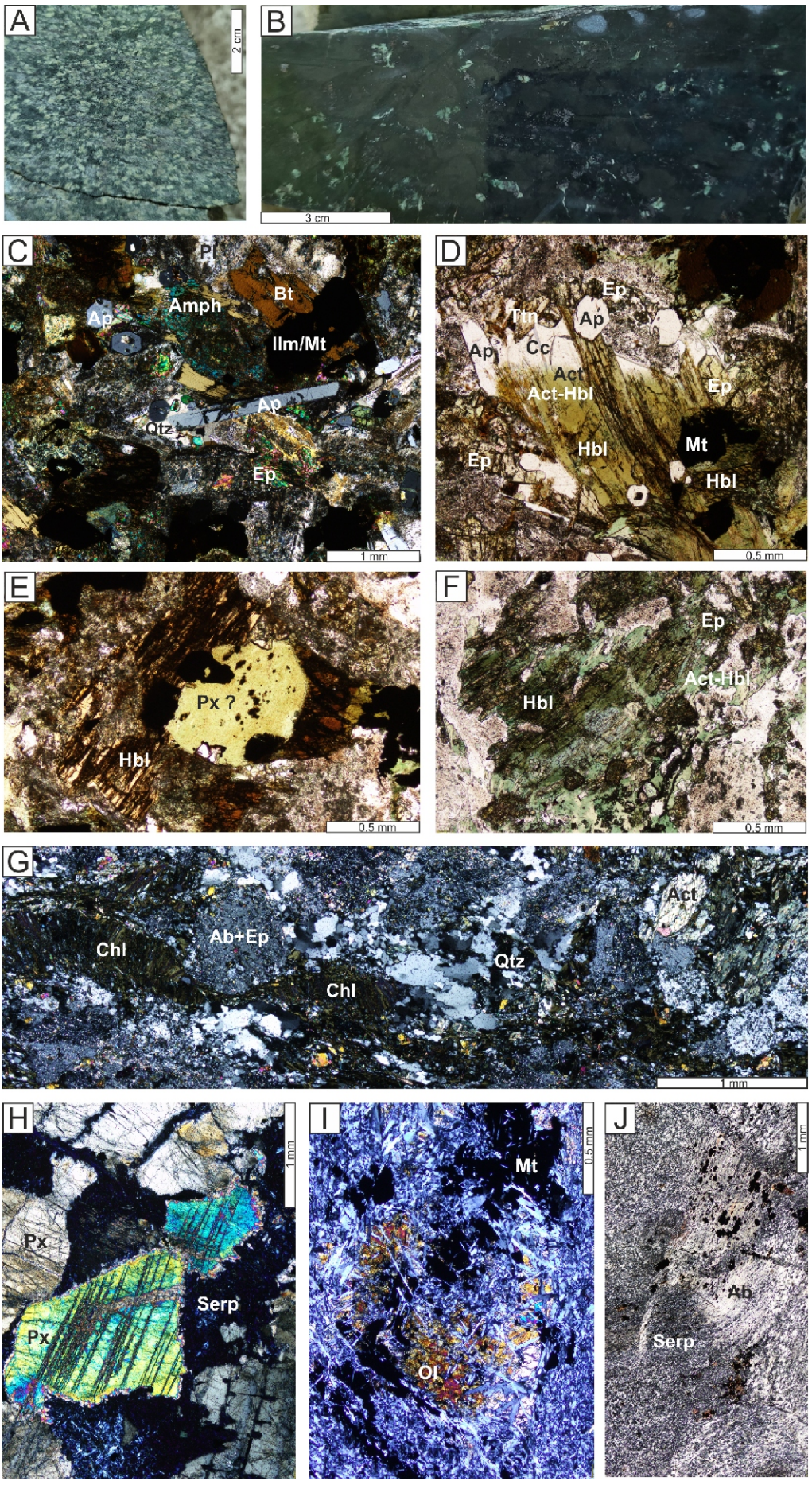
A
2 cm
B
3 cm
C
Pl
Amph
Bt
Ap
Ilm/Mt
Ap
Qtz
Ep
1 mm
D
Ep
Ttn
Ap
Ap
Cc
Act
Act-Hbl
Ep
Hbl
Mt
Ep
Hbl
0.5 mm
E
Px ?
Hbl
0.5 mm
F
Ep
Act-Hbl
Hbl
0.5 mm
G
Act
Chl
Ab+Ep
Qtz
Chl
1 mm
H
1 mm
Px
Serp
Px
I
0.5 mm
Mt
Ol
J
1 mm
Ab
Serp

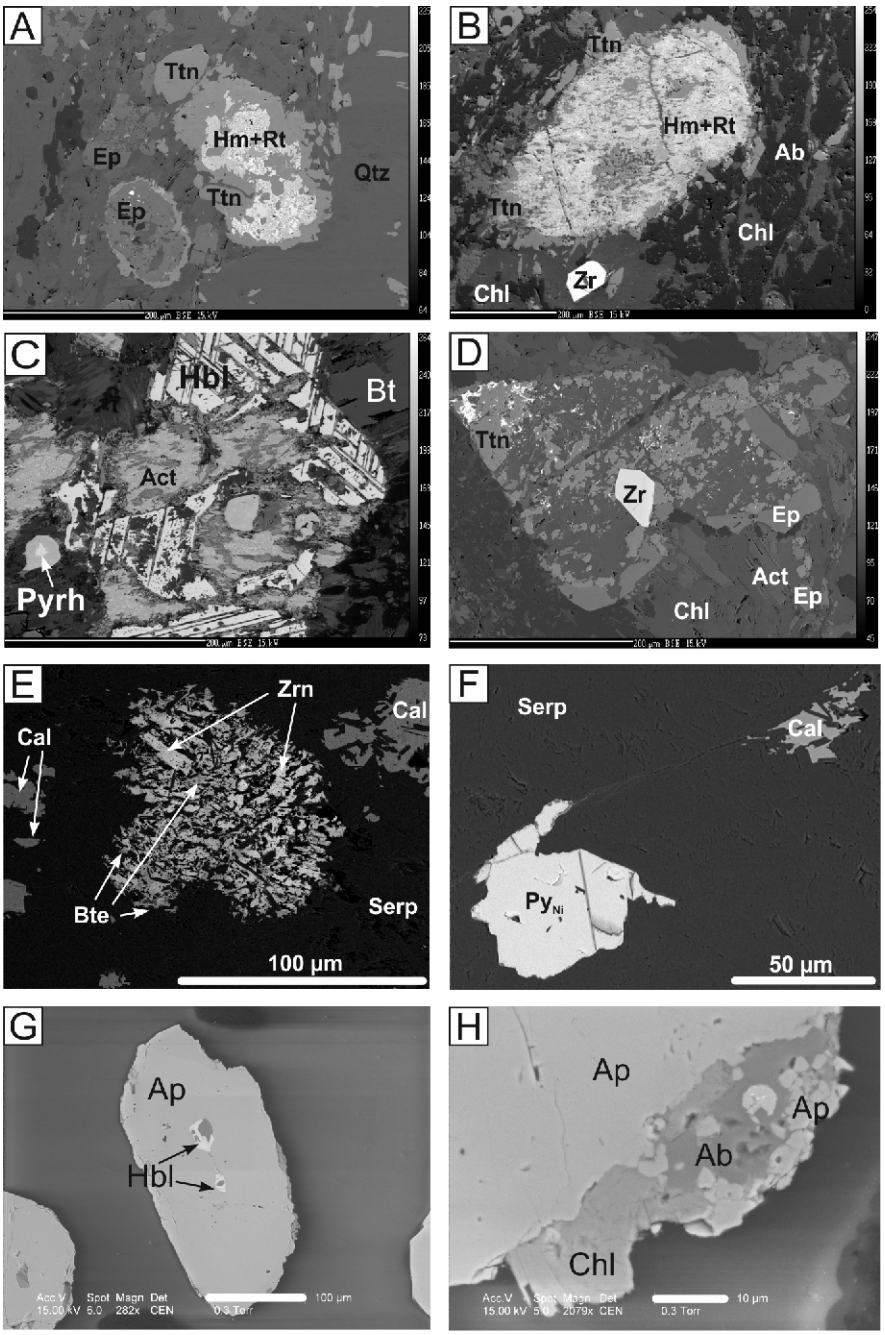

Fig. 4. BSE images of mineral assemblages from mafic exotic blocks

A – pseudomorphs composed of epidote + titanite and hematite + rutile rimmed by titanite; **B** – hematite+rutile +titanite pseudomorphs enclosed in albite+chlorite matrix; **C** – high-Ti hornblende consumed by actinolite and biotite; note the pyrrhotite crystal partially replaced by goethite; **D** – titanite+ chlorite+epidote assemblage enclosing zircon; **E** – skeletal zirconolite and baddeleyite intergrowths in the serpentinite; **F** – high-Ni pyrite crystal in serpentinite; **G** – inclusion of hornblende in apatite; **H** – rim of the apatite crystal with co-crystallizing apatite+albite+chlorite; Bte – baddeleyite, Hm – hematite, Qtz – quartz, Rt – rutile, Zr – zircon, Zrn – zirconolite, other explanations as on Figure 3

Fig. 3. Textures and microtextures of basic exotic rocks from Osielec olistostrome

A – field photograph of the gabbro (D5); **B** – photograph of the polished surface of serpentinite (D10); **C** – coarse grained metagabbro (D5) with relics of primary minerals (plagioclase and ilmenite/magnetite) and secondary ones: apatite, epidote, biotite, quartz; **D** – secondary alterations of metagabbro (D5) components, with gradual replacement of magmatic hornblende by secondary amphiboles (actinolite) and apatite + calcite + epidote + titanite assemblage; note the inclusions of amphiboles and plagioclases in apatite in C and D; **E** – chlorite-amphibole pseudomorph (pyroxene ?); **F** – Actinolite-hornblende and epidote rims on hornblende; **G** – banded rock (D4; "prasinite" *sensu* Wieser, 1952), composed of interleaving bands of chlorite and epidote + albite + quartz with local patches of actinolite; **H** – partially serpentinized pyroxene crystals in serpentinite (D10); **I** – olivine remnants in serpentinite (D10); **J** – ghost-structures in serpentinite (D10) with albitic pseudomorphs after deformed plagioclases (C, G, H, I - crossed polarized light; D, E, F – plane polarized light); Ab – albite, Act – actinolite, Amph – amphibole, Ap – apatite, Cc – calcite, Chl – chlorite, Ep – epidote,Hbl – hornblende, Ilm – ilmenite, Mt – magnetite, Ol – olivine, Pl – plagioclase, Px – pyroxene, Serp – serpentine, Ttn – titanite

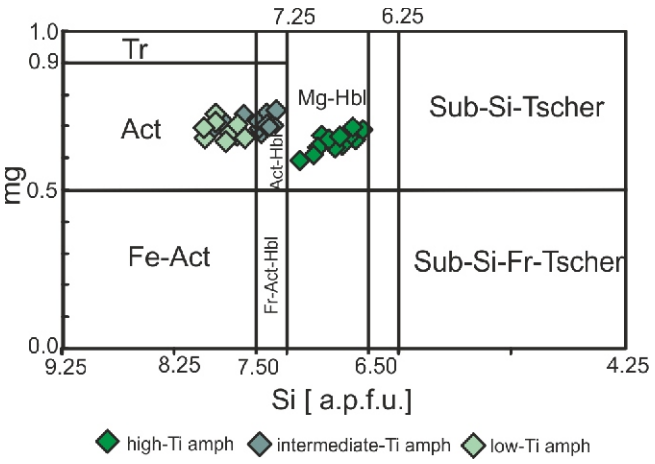

Fig. 5. Classification of analysed amphibole grains in #mg *versus* Si [a.p.f.u.] according to Leake et al. (1998)

Fe-Cr spinel and magnetite are partly replaced by hematite. Grains of millerite and Ni-pyrite associated with baddeleyite and zirconolite intergrowths are dispersed inside the serpentine matrix (Fig. 4E, F).

APATITE U-Pb LA ICP-MS DATING

Apatite crystals from D5 sample are clear, translucent and idiomorphic hexagonal prisms, with aspect ratios ranging from 2:1 to 6:1 and width ranging from 60 to 220 mm. One hundred and four analyses from 48 grains yield an unanchored Tera-Wasserburg lower intercept age of 613.92 ±3.14 Ma with a $^{207}Pb/^{206}Pb$ initial ratio of 0.8583 ±0.0087 (MSWD = 2.5; Fig. 7 and Appendix 2).

WHOLE ROCK GEOCHEMISTRY

Two newly analysed samples of the prasinite and altered gabbro (D4 and D5) are similar in chemical composition with

Table 1

Chemical composition and crystal-chemical formulae of amphiboles from the mafic exotic blocks (D4 and D5) from Osielec village (Magura Nappe)

Sample	LoD	high-Ti amphiboles (D5)				intermediate (D5)		low-Ti amphiboles		
		H#1	H#2	H#3	H#4	D5_I#1	D5_I#2	D5#1	D4#2	D4#3
SiO_2	0.02	46.98	46.84	46.49	47.38	49.37	50.15	53.35	53.09	55.42
TiO_2	0.03	1.22	1.33	1.58	1.11	0.85	0.29	0.02	0.07	0.04
Al_2O_3	0.01	6.97	6.79	7.01	6.62	6.07	5.11	1.85	2.85	1.13
Cr_2O_3	0.01	0.04	b.d.l.	0.01	0.02	0.01	b.d.l.	0.02	b.d.l.	b.d.l
FeO	0.07	15.83	16.28	16.01	15.92	15.49	15.58	13.38	14.21	13.25
MnO	0.06	0.47	0.52	0.59	0.43	0.45	0.48	0.34	0.41	0.27
MgO	0.02	12.09	12.02	12.05	12.21	11.47	13.34	15.09	14.22	15.66
CaO	0.02	11.62	12.01	11.62	12.10	11.47	12.16	12.29	11.85	12.47
Na_2O	0.02	0.93	0.89	0.93	0.77	0.95	0.73	0.40	0.71	0.38
K_2O	0.01	0.63	0.64	0.64	0.60	0.54	0.31	0.06	0.12	0.05
Cl	0.02	0.04	0.04	0.06	0.16	0.24	0.02	b.d.l	b.d.l	b.d.l.
TOTAL										
Fe_2O_3*		4.73	4.18	5.24	3.73	0.64	4.49	2.18	2.47	1.35
FeO*		11.58	12.52	11.30	12.56	14.92	11.54	11.42	12.00	12.03
H_2O*		2.02	2.01	2.01	2.02	2.01	2.06	2.06	2.07	2.11
Crystal-chemical formulae based on 13-CNK										
Si		6.955	6.934	6.882	7.007	7.327	7.267	7.746	7.671	7.878
Al^{IV}		1.045	1.066	1.118	0.993	0.673	0.733	0.254	0.329	0.122
M1, M2, M3-site										
Al^{VI}		0.172	0.119	0.106	0.161	0.388	0.140	0.062	0.157	0.067
Ti		0.136	0.149	0.176	0.123	0.095	0.031	0.002	0.007	0.005
Cr^{3+}		0.004	–	0.001	0.003	0.002	–	0.003	0.000	0.000
Fe^{3+}		0.527	0.466	0.584	0.415	0.071	0.490	0.239	0.268	0.144
Fe^{2+}		1.433	1.549	1.399	1.553	1.851	1.398	1.386	1.449	1.430
Mn		0.058	0.065	0.074	0.054	0.057	0.058	0.042	0.050	0.032
Mg		2.669	2.653	2.659	2.691	2.537	2.882	3.266	3.063	3.317
M4-site										
Ca		1.843	1.905	1.843	1.917	1.824	1.888	1.912	1.835	1.899
Na		0.157	0.095	0.157	0.083	0.176	0.112	0.088	0.165	0.096
A - site										
Na		0.131	0.160	0.111	0.138	0.098	0.094	0.024	0.033	–
K		0.118	0.121	0.120	0.113	0.102	0.058	0.010	0.022	0.008
Cl		0.010	0.011	0.014	0.009	0.012	0.005	–	–	–
OH		1.990	1.989	1.986	1.991	1.988	1.995	1.998	1.999	2.000
#mg		0.651	0.631	0.655	0.634	0.578	0.673	0.702	0.679	0.699
$Fe^{3+}/(Fe^{3+}+Al^{VI})$		0.754	0.797	0.846	0.721	0.155	0.777	0.793	0.631	0.683
amphibole name		Mg-Hbl	Mg-Hbl	Mg-Hbl	Mg-Hbl	Act-Hbl	Act-Hbl	Act	Act	Act
P [MPa]		111	106	112	101	–	67	30	–	
T [°C]		787	792	797	782	733	732	652	662	630

LoD – limits ondetection; #mg – Mg/(Mg+Fe) in molecular units; * calculated values according to Ridolfi et al. (2010) procedure

Table 2

Chemical composition and crystal-chemical formulae of titanite and epidote from gabbroic exotic blocks from Osielec

Compound (wt.%)	LoD	Epidote			Titanite		
		Ep#1(D5)	Ep#2(D4)	Ep#3(D4)	Ttn#1(D5)	Ttn#2(D5)	Ttn#3(D4)
V_2O_5	0.06	0.22	b.d.l	b.d.l.	0.10	0.11	0.43
Nb_2O_5	0.08	–	–	–	0.11	0.36	0.08
SiO_2	0.05	37.46	37.29	37.71	30.62	30.41	30.39
TiO_2	0.03	0.18	0.15	0.11	37.72	37.71	38.02
Al_2O_3	0.01	22.17	21.53	24.09	0.78	1.07	1.13
Fe_2O_3	0.08	13.78	15.81	12.06	0.96	0.90	1.22
CaO	0.03	22.96	23.38	23.84	28.83	28.39	28.65
SrO	0.05	0.14	0.12	0.15	–	–	–
BaO	0.05	0.07	b.d.l	0.07	–	–	–
MnO	0.06	0.24	0.10	0.17	0.14	0.15	0.08
$H_2O^c_{alc}$	–	1.86	1.87	1.84	–	–	–
F	0.03	b.d.l.	b.d.l.	b.d.l.	0.92	0.25	0.14
O=F		–	–	–	0.39	0.10	0.06
Total		99.66	100.25	99.82	99.6	100.61	100.14
a.p.f.u.		formula based on 25 O^{2-}			formula based on 18 O^{2-}		
V^{5+}		0.029	–	–	0.010	0.010	0.034
Nb^{5+}		–	–	–	0.006	0.019	0.004
Si^{4+}		6.032	5.999	6.060	3.632	3.620	3.580
Ti^{4+}		0.022	0.020	0.014	3.453	3.376	3.368
Al^{3+}		4.208	4.072	4.090	0.109	0.151	0.156
Fe^{3+}		1.669	1.910	1.930	0.086	0.080	0.108
Ca^{2+}		3.961	4.015	3.810	3.664	3.621	3.616
Sr^{2+}		0.013	0.012	0.014	–	–	–
Ba^{2+}		0.005	–	0.005	–	–	–
Mn^{2+}		0.033	0.016	0.022	0.015	0.015	0.008
F		–	–	–	0.343	0.093	0.051
$\sum_{cations}$		15.98	16.044	15.93	10.969	10.985	10.874

Table 3

Chemical composition and crystal-chemical formulae of ilmenite and rutile from gabbroic exotic blocks (D5)

Compound	LoD	Ilm #1	Ilm #2	Rt #1	Rt #2
TiO_2	0.03	51.98	52.24	95.63	91.38
V_2O_3	0.07	0.26	0.22	0.82	0.54
Cr_2O_3	0.02	b.d.l	0.04	b.d.l.	0.14
Fe_2O_3	0.06	–	–	3.08	7.99
FeO	0.02	34.96	39.72	–	–
MnO	0.05	11.86	6.74	–	–
MgO	0.05	0.12	0.15	–	–
Total		99.19	99.11	99.53	100.05
		Ilm formula ($3O^{2-}$)		Rt formula ($2O^{2-}$)	
Ti		0.994	0.990	0.954	0.931
V		0.005	0.005	0.009	0.006
Cr		–	0.001	–	0.001
Fe^{3+}		–	–	0.031	0.081
Fe^{2+}		0.740	0.838	–	–
Mn		0.255	0.148		
Mg		0.004	0.006		

previously analysed metagabbro and prasinite samples, with SiO_2 content in the range of 57.6–58.3 wt.%, metaluminous (ASI = 0.79–1.03), rich in Mg (#mg = 0.64–0.66; Gawęda et al., 2019: tables 6 and 7). Their chondrite (C1)-normalized REE patterns show almost no fractionation (Ce_N/Yb_N = 0.88–0.91; Eu/Eu* = 0.89–0.92; Table 6 and Fig. 8A; compare Gawęda et al., 2019). The serpentinised sample (D10) is poor in SiO_2 and rich in Mg (#mg = 0.95), characterised by flat chondrite-normalized REE patterns (Ce_N/Yb_N = 0.94; Eu/Eu* = 0.88; Table 6 and Fig. 8A). All analysed rocks have stable Nd/Th ratio (4.00–4.74; Table 6). Assuming a ~614 Ma age of intrusion (Gawęda et al., 2019) the initial $^{143}Nd/^{144}Nd$ ratio range from 0.512083 to 0.512107 in the case of altered gabbro and prasinite (D4 and D5 samples respectively) and 0.511989 for serpentinite, while e_{Nd} (614 Ma) is positive in all samples (4.62 and 5.09 in gabbros, 2.79 in serpentinite; Table 7). Initial $^{87}Sr/^{86}Sr$ ratios (I_{Sr}^{614}) are 0.704366 and 0.702871 for D4 and D5 samples, respectively, while the serpentinized rock (D10) shows disturbance of the Sr radiogenic system (Table 7).

Table 4

Representative EMPA analyses of chlorite with their crystal-chemical formulae from the D5 (#1–#5) and D10 (#6–#10) samples

Sample no.	LoD	D5 ("prasinite")					D10 (serpentinite)				
Compound		Ch#1	Ch#2	Ch#3	Ch#4	Ch#5	Ch#6	n#7	n#8	n#9	n#10
SiO_2	0.02	24.58	24.79	24.88	24.81	25.11	25.45	25.35	25.44	25.11	29.29
TiO_2	0.02	b.d.l.	b.d.l.	b.d.l.	b.d.l.	b.d.l.	0.09	b.d.l.	0.06	b.d.l.	0.37
Al_2O_3	0.01	20.71	20.41	20.27	20.70	16.73	20.45	20.71	20.82	16.73	17.69
$Fe_2O_3^*$	–	0.63	0.49	0.35	0.64	b.d.l.	0.46	0.64	0.15	b.d.l.	2.37
FeO	0.04	30.87	32.45	32.70	32.11	33.36	29.33	28.51	30.57	29.09	26.69
MnO	0.09	0.35	0.39	0.44	0.40	0.28	0.46	0.42	0.38	0.40	0.34
MgO	0.01	9.57	9.47	9.61	9.43	9.69	11.85	11.83	12.11	12.10	11.21
CaO	0.05	0.16	b.d.l.	b.d.l.	b.d.l.	b.d.l.	0.06	b.d.l.	b.d.l.	0.06	0.23
H_2O^*	–	10.86	10.94	10.96	10.95	10.48	11.14	11.09	11.28	10.48	11.29
Total		**97.73**	**98.94**	**99.22**	**99.03**	**95.65**	**99.29**	**98.55**	**100.80**	**93.97**	**99.48**
crystal-chemical formula based on 28 O^{2-}. Fe^{2+}/Fe^{3+} and OH^- calculated assuming full site occupancy											
Si		5.41	5.43	5.44	5.42	5.74	5.46	5.46	5.40	5.72	6.13
Al^{iv}		2.59	2.57	2.56	2.58	2.26	2.54	2.54	2.60	2.28	1.87
Al^{vi}		2.80	2.70	2.66	2.75	2.25	2.64	2.72	2.61	2.22	2.55
Ti		–	–	–	–	–	0.02	–	0.01	–	0.06
Fe^{3+}		0.10	0.08	0.06	0.10	–	0.07	0.10	0.02	–	0.37
Fe^{2+}		5.68	5.94	5.98	5.86	6.38	5.26	5.13	5.43	5.57	4.67
Mn		0.06	0.07	0.08	0.07	0.05	0.08	0.08	0.07	0.08	0.06
Mg		3.14	3.09	3.13	3.07	3.30	3.79	3.80	3.83	4.11	3.50
Ca		0.04	–	–	–	–	0.01	–	–	0.02	0.05
OH*		16.00	16.00	16.00	16.00	16.00	16.00	16.00	16.00	16.00	16.00
Fe/Fe+Mg		0.65	0.66	0.66	0.66	0.66	0.58	0.58	0.59	0.58	0.59
T_1 [°C]		355	352	351	354	302	347	348	357	305	238
T_2 [°C]		344	341	340	343	291	336	337	346	295	229
T_3 [°C]		341	340	339	341	306	331	331	337	303	260

LoD – Limits on detection; * calculated values

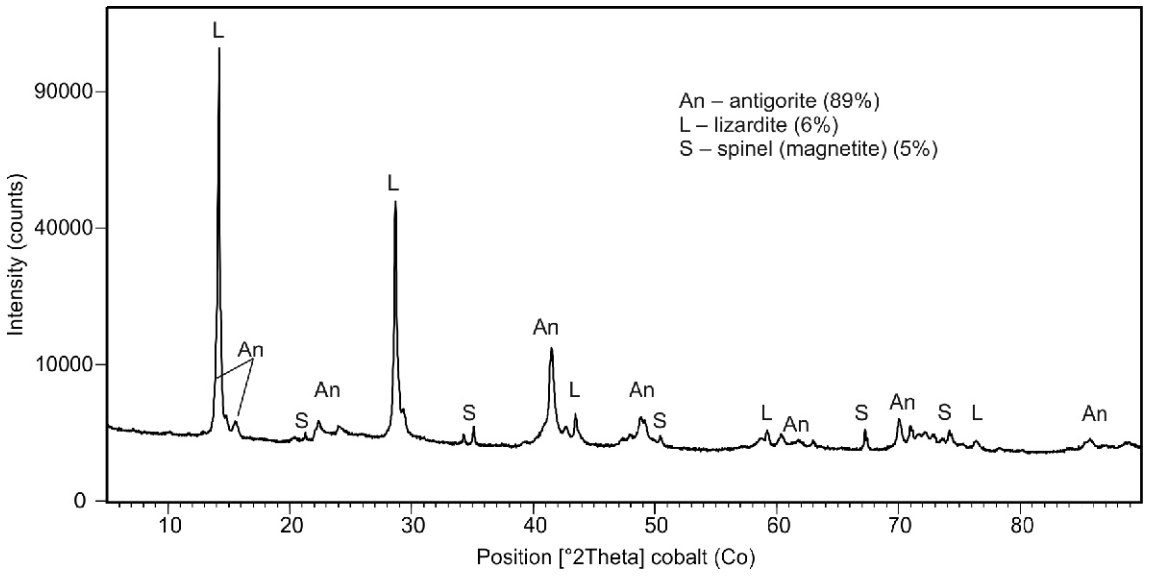

Fig. 6. X-ray diffraction patterns and semi-quantitative analysis (in wt.%) of mineral phases, composing D10 sample (serpentinite) using the Rietveld method

Table 5

Representative micro-chemical analyses of olivine (Ol) and pyroxene (Px) and their crystal-chemical formulae (D10)

Sample no.	LoD	olivine			pyroxene					
		Ol#1	Ol#2	Ol#3	(Al,Cr) diopside (core)			diopside (rim)		
					Px#1	Px#2	Px#3	Px#4	Px#5	Px#6
SiO_2	0.02	41.16	41.17	41.27	51.91	51.92	51.78	55.03	55.26	55.12
TiO_2	0.01	0.03	0.05	0.02	0.58	0.58	0.48	0.05	b.d.l.	0.01
Al_2O_3	0.01	b.d.l.	0.04	b.d.l.	4.98	5.16	4.53	0.02	b.d.l.	0.05
V_2O_3	0.02	b.d.l.	b.d.l.	b.d.l.	0.10	0.10	b.d.l.	b.d.l.	b.d.l.	b.d.l.
Cr_2O_3	0.01	0.01	0.02	0.02	0.66	0.63	0.62	0.12	0.02	0.14
FeO	0.08	10.43	10.28	10.35	2.77	2.93	2.91	2.43	1.28	2.54
MnO	0.05	0.71	0.66	0.65	0.09	0.11	0.15	0.13	0.13	0.09
NiO	0.06	0.21	0.25	0.25	0.11	b.d.l.	b.d.l.	0.06	b.d.l.	b.d.l.
MgO	0.02	48.02	47.75	48.13	15.13	15.20	16.15	17.05	17.81	17.23
CaO	0.04	b.d.l.	b.d.l.	b.d.l.	22.99	22.83	22.14	25.40	25.89	25.38
Na_2O	0.03	b.d.l.	b.d.l.	b.d.l.	0.93	0.82	0.59	b.d.l.	b.d.l.	0.05
Total		100.57	100.32	100.69	100.25	100.28	99.35	100.29	100.29	100.61
		formula unit per 4 O^{2-}			formula unit per 6 O^{2-}					
Si		1.007	1.010	1.008	1.888	1.885	1.894	1.999	2.002	1.996
Ti		0.001	0.001	0.000	0.016	0.016	0.013	0.001	–	–
Al		–	0.001	0.000	0.213	0.221	0.195	0.001	–	0.002
V		–	–	–	0.003	0.003	–	–	–	–
Cr		–	0.000	0.000	0.019	0.018	0.018	0.004	0.001	0.004
Fe2+		0.213	0.211	0.211	0.084	0.089	0.089	0.074	0.038	0.077
Mn		0.015	0.014	0.013	0.003	0.003	0.005	0.004	0.004	0.003
Ni		0.004	0.005	0.005	0.003	–	–	–	–	–
Mg		1.751	1.746	1.753	0.82	0.822	0.88	0.923	0.955	0.928
Ca		–	–	–	0.896	0.888	0.868	0.989	0.998	0.987
Na		–	–	–	0.066	0.058	0.042	–	–	0.003

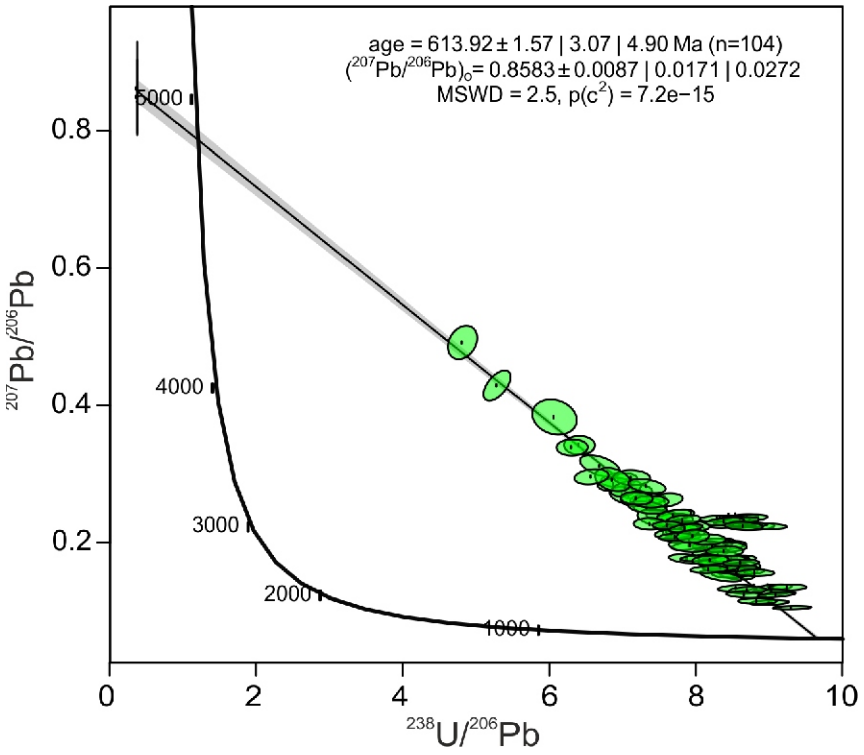

Fig. 7. U-Pb concordia plot of the apatite from Osielec gabbroic rock

Table 6

Chemical composition and selected petrological indices of the whole-rock samples of crystalline exotic blocks

Sample no.	D4	D5	D10
major elements			
SiO_2	58.31	57.82	39.62
TiO_2	0.83	0.95	0.10
Al_2O_3	16.19	17.19	2.80
Fe_2O_{3T}	6.98	7.48	7.63
MnO	0.12	0.13	0.12
MgO	3.17	3.62	37.8
CaO	7.03	4.99	0.21
Na_2O	4.57	3.91	0.03
K_2O	0.47	1.58	0.01
P_2O_5	0.20	0.24	0.00
LOI	2.74	2.77	11.72
Total	100.61	100.68	100.04
trace elements [ppm]			
Sr	493.0	325.1	1.7
Ba	128.0	367.0	4.0
Rb	13.3	46.3	0.1
Th	3.9	4.6	0.1
U	1.2	1.3	0.1
Ga	17.8	19.1	1.6
Ni	23.7	21.7	1234.4
Cr	68.40	63.60	3079.12
Zr	180.60	162.90	4.60
Hf	4.50	4.50	0.10
Y	19.20	18.60	1.80
Nb	5.40	6.80	0.50
Ta	0.50	0.50	0.10
La	15.10	15.50	0.40
Ce	32.40	32.90	0.70
Pr	4.42	4.47	0.60
Nd	18.50	18.80	0.40
Nd	3.99	4.23	0.15
Eu	1.13	1.21	0.05
Gd	3.76	3.81	0.12
Tb	0.57	0.59	0.04
Dy	3.24	3.48	0.28
Ho	0.67	0.70	0.07
Er	1.96	2.05	0.02
Tm	0.30	0.29	0.03
Yb	1.92	1.95	0.20
Lu	0.27	0.28	0.03
Nd/Th	4.74	4.09	4.00
REE	88.23	90.26	2.81
Eu/Eu*	0.89	0.92	0.88
$lowCe_N/Yb_N$	4.55	4.55	0.94
Nb/La	0.36	0.44	1.25

Eu/Eu* = Eu/ (Sm · Gd)

Table 7

Sm-Nd and Rb-Sr whole rock isotopic data from the mafic crystalline exotic blocks from Osielec

Sample no.	$^{143}Nd/^{144}Nd$	2	$^{147}Sm/^{144}Nd$	$(^{143}Nd/^{144}Nd)_{614}$	ε_{614}	ε_0	T_{DM}	$^{87}Sr/^{86}Sr$	2	$^{87}Rb/^{86}Sr$	$^{87}Sr/^{86}Sr_{614}$
D4	0.512632	0.000004	0.130391099	0.512106989	5.09	–0.12	0.86	0.705041	0.000003	0.077042	0.704366
D5	0.512630	0.000004	0.136028265	0.512082942	4.61	–0.15	0.90	0.706433	0.000003	0.406711	0.702871
D10	0.512902	0.000005	0.226728284	0.511989487	2.79	5.15	1.04	0.710023	0.000004	0.167986	0.708552

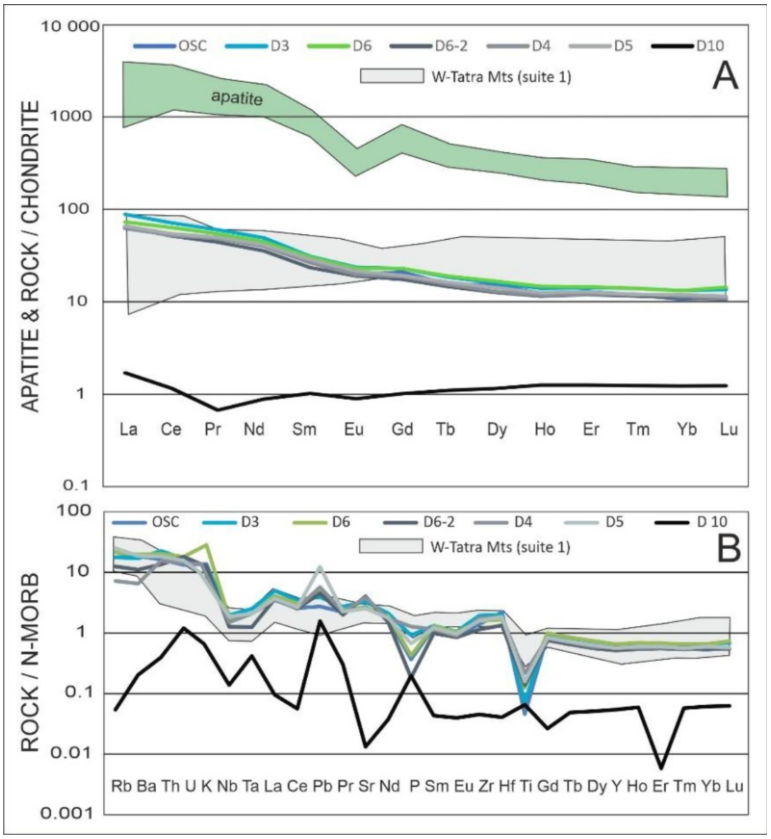

Fig. 8A – trace elements plot chondrite-normalised (C1) REE patterns of mafic rock varieties from the Osielec olistostrome (D4, D5, D10 and formerly analysed OSC, D3, D6, D6-2) and apatite from gabbroid rock (D5); B – N-MORB normalized multi-element patterns of mafic rocks varieties from Osielec (including formerly published analyses from Gawęda et al., 2019)

DISCUSSION

PETROGENETIC CHARACTER OF THE EXOTIC BLOCKS

Mafic magmatic rocks are considered as reliable markers for constraining tectonic setting. However, many factors (fractionation, contamination, fluid influx) can modify the primary geochemical and isotopic composition, and could caused complex interpretation (Pearce, 2008; Xia and Li, 2019 and references therein).

Due to the intensive geochemical alteration (including disturbance of their Sr isotopic signatures) observed in the serpentinite fragments (Fig. 8B and Table 7), only gabbroic rocks were used to interpret the tectonic setting. Crustal contamination is shown by negative Nb, Ta, P and especially Ti anomalies on N-MORB–normalised multielement diagram (Fig. 8B) and the low Nb/La ratios (Xia and Li, 2019) in the range of 0.30–0.44 (Table 6). This suggests either an arc setting (Fig. 9A, B) or crustal contamination of within plate (continental) basalts (Fig. 9C, D).

The source magma may be of depleted character (Fig. 9E), and was likely modified by subduction, with lithospheric mantle input (SZLM; Fig. 9A) and underwent subsequent fractionation with significant residual garnet (Pearce et al., 2021). As all samples plot in low-TiO_2/Yb and relatively high Th/Nb SZLM array (Pearce et al., 2021), we can infer plume-crust interaction or plume-interaction with subduction.

Taking into account the U-Pb zircon crystallization age of the mafic rocks (613.3 ±2.6 Ma for massive gabbro-diorite and 614.6 ±2.5 Ma for layered “prasinite”; Gawęda et al., 2019), which almost identical with U-Pb apatite age (613.92 ±1.57 Ma; Appendix 2 and Fig. 7), Neoproterozoic rifting in the back-arc regime can be assumed (Fig. 11).

NATURE OF THE METAMORPHISM

The mineral assemblages in the gabbroic rocks document the history of cooling and alteration. All amphibole group minerals represent a low-pressure assemblage and reveal the wide spectrum of crystallization temperatures: from high-Ti Mg-hornblende (797 to 767°C, 112–95 MPa; Table 1) through intermediate Mg-hornblendes (738 to 652°C at 68–30 MPa; Table 1) to low-Ti amphiboles (actinolitic hornblende to actinolite), typical of ocean floor/hydrothermal metamorphism, crystallizing in the temperature range of 664–630°C and less, at very low pressures (Table 1 and Fig. 10; Silantyev et al., 2008). Rock textures and mineral assemblages suggest that apatite co-crystallize with actinolite and calcite, but after hornblende and plagioclase (Figs. 3D and 4G, H), while apatite trace element chemistry demonstrate the primary magmatic character (Fig. 8A). The available evidence implies rapid cooling and apatite re-crystallization in the stability field of actinolite + albite + epidote + titanite + chlorite + calcite, as a result of calcium redistribution and alteration by hydrothermal fluids and replacement

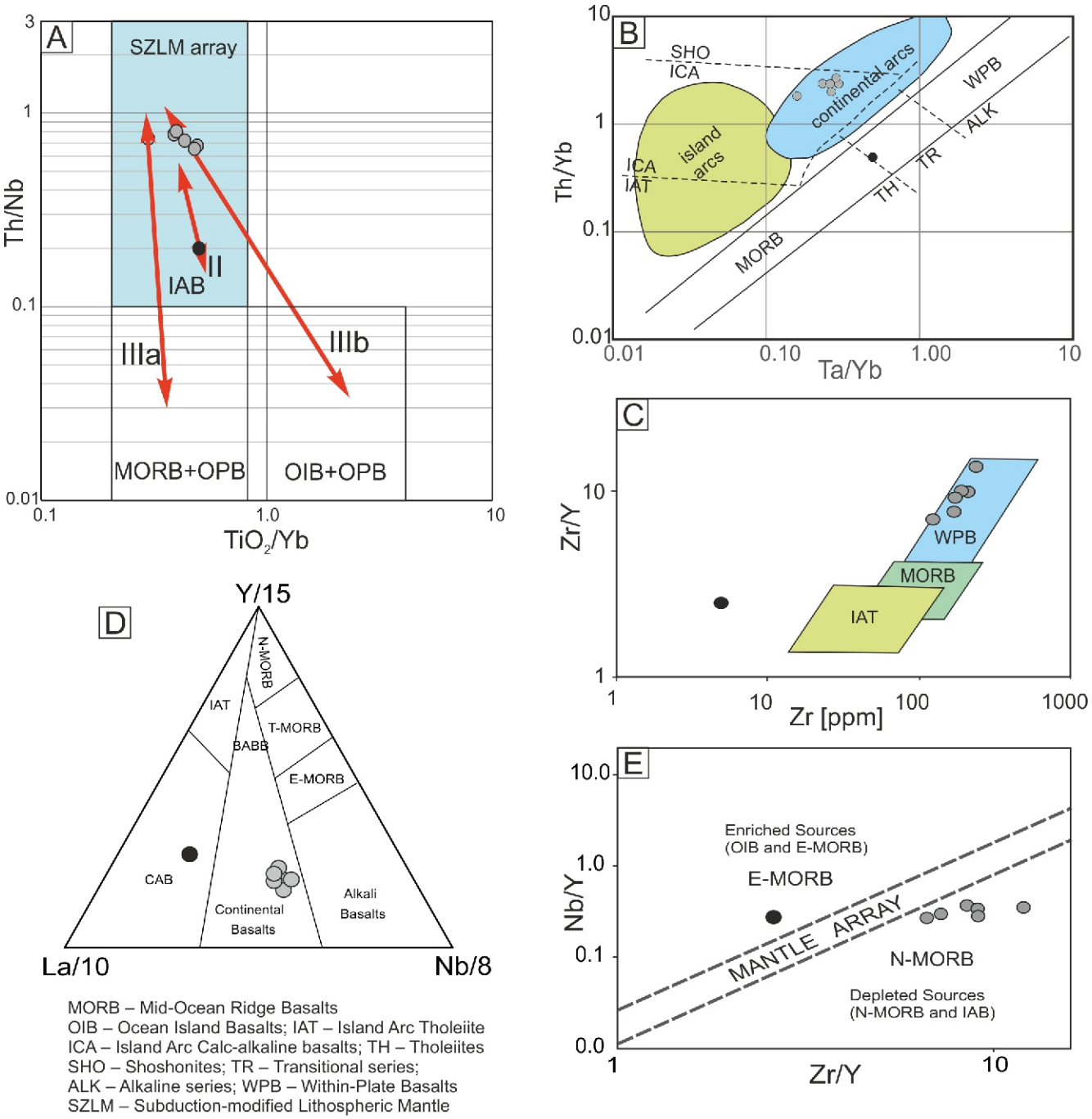

Fig. 9. Classification diagrams of mafic rocks from the Osielec olistostrome

A – plot in the LIP (Larg Igneous Provinces) printing diagram (after Pearce et al., 2021); **B** – Th/Yb *versus* Ta/Yb diagram (after Pearce, 1982), Zr/Ti–Nb/Y diagram from Winchester and Floyd (1977); **C** – Zr *versus* Zr/Y tectonic discrimination diagram (after Pearce and Norry, 1979); **D** – La/10–Y/15–Nb /8 after Cabanis and Lecolle (1989); **E** – Nb/Y *versus* Zr/Y with mantle array separating enriched from depleted sources (after Fitton, 2007); other explanations as in Figure 7

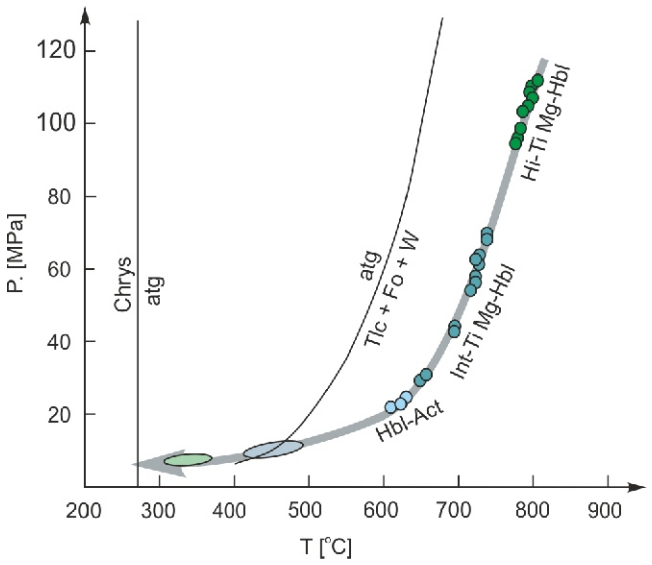

Fig. 10. Pressure-temperature cooling path for mafic rocks from Osielec olistostrome

of the primary Ca-bearing minerals by low temperature assemblage (Schwarzenbach and Steele-MacInnis, 2020). We can assume that the U-Pb apatite age documents an age of post-magmatic recrystallization connected with pervasive Ca mobility. The apatite U-Pb age (613.9 ±1.6 Ma; Appendix 2 and Fig. 7), identical with zircon U-Pb age (Gawęda et al., 2019), implies a rapid cooling of the magma.

Some parts of the samples (banded rocks/prasinite *sensu* Wieser, 1952) show intensive shearing with the shear-bands defined by the chlorite and chlorite-epidote-titanite-quartz bands (Fig. 3G). Consequently, we can assume that some portions of the mafic complex underwent shearing.

The serpentinite with relic olivine, pyroxene and typical accessory minerals (baddeleyite, zirconolite, Ni-pyrite, pyrrhotite) documents the pervasive alteration of the ultramafic portion of an ophiolite sequence, likely portions of hydrated mantle, associated with slow spreading ridges (Cannat, 1993). As documented by Mével (2003) serpentinization of mantle-derived ultramafic rocks starts in relatively high temperatures (500–300°C) and sea-water is the main fluid, causing hydration and oxidation (e.g. formation of magnetite). Antigorite, which is the main component of the serpentinite investigated herein, is stable at high temperatures (up to 500°C; Evans et al., 1976),

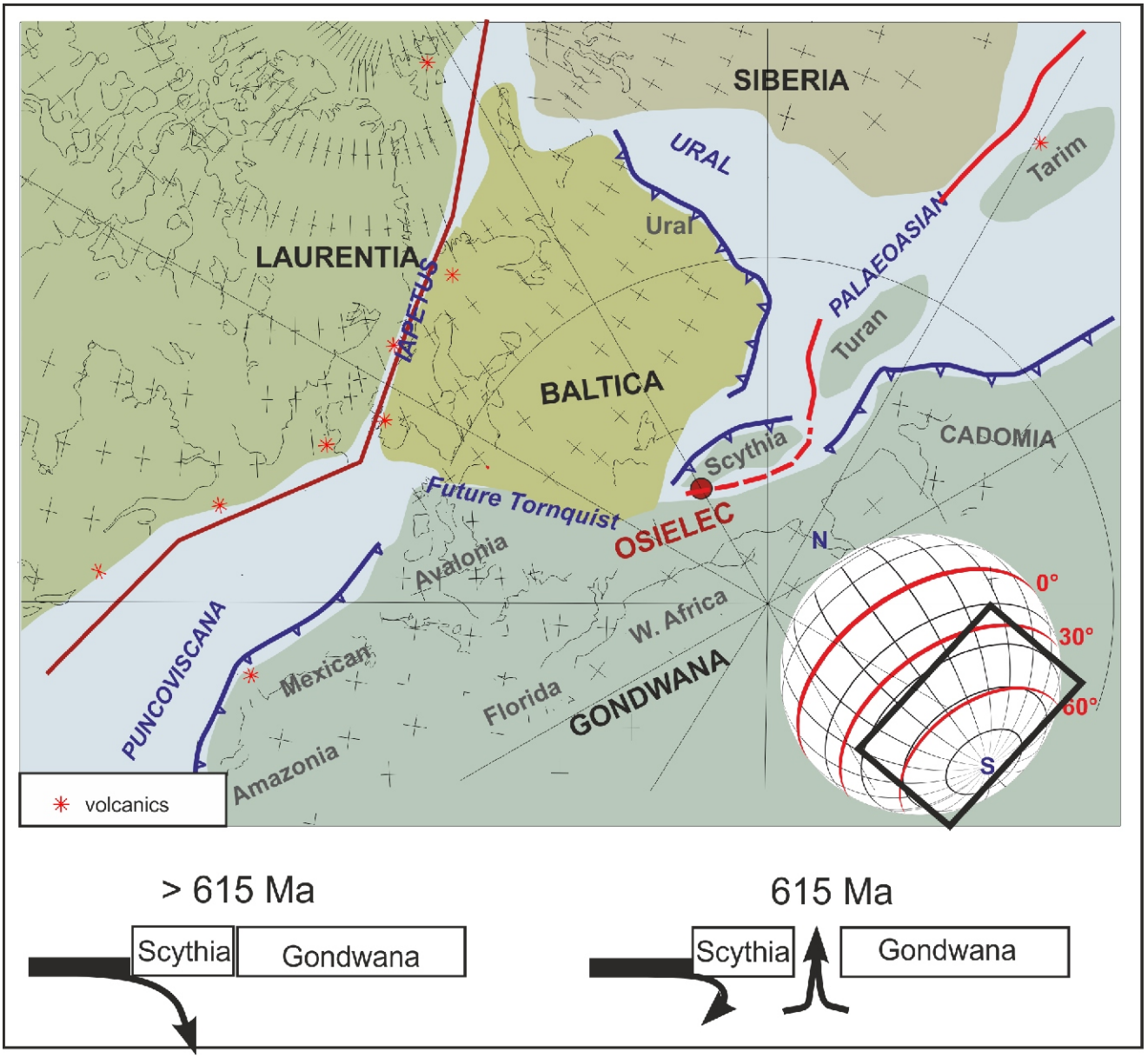

Fig. 11. Plate tectonic map of Pannotia at ~600 Ma (stereographic projection) with the simplified graphs, showing possible scenarios before ~615 Ma and at ~615 Ma for the Osielec mafic rocks, modified from Golonka and Gawęda (2012) and Gawęda et al. (2017)

while lizardite, forming at low temperatures is subordinate and can be assumed as secondary phase, which together with chlorite and calcite are likely a result of low temperature interaction of the sea water with rocks (Gibbson et al., 1996). The temperature of chlorite crystallization was calculated by using three various empirical chlorite geothermometers proposed by Cathelineau and Nieva (1985), Kranidiotis and MacLean (1987), and Jowett (1991; Table 4). The temperatures range of 230–360°C (Fig. 10) is in agreement with published data on the temperature conditions of the serpentinization at mid-ocean ridges (Mével, 2003 and references therein).

IMPLICATION FOR NEOPROTEROZOIC PALAEOGEOGRAPHY

The exotic rocks fragments, dated at ~614 Ma, represent probably the remnants of a mantle plume (within plate magmas), characterised by very strong lithospheric contamination (expressed by low Nb/La ratios; Xia and Li, 2019; Fig. 9A, C–E and Table 6). Such an interpretation requires an assumption of the initial ocean floor formation. That is documented by almost identical (within the uncertainty) U-Pb crystallization age of zircon and cooling age of apatite (Fig. 5 and Appendix 2; Gawęda et al., 2019), and documented hydrothermal metamorphism.

The late Neoproterozoic is a time of Rodinia/Pannotia break-up and formation of the Iapetus and Tornquist oceans (e.g., Weber et al., 2020 and references therein; Murphy et al., 2021 and references therein; Robert et al., 2021). The first phase of rifting, which lasted from 750 to 700 Ma led to the Western Iapetus/Puncoviscana Ocean formation (Robert et al., 2021). Formation of the Central Iapetus Magmatic Province (CIMP; so-called Eastern Iapetus), as a second phase, took place in a time span of 635–550 Ma, in two stages. The first stage, from 620 to 600 Ma (Gumsley et al., 2020), was characterised by continental tholeiitic magmatism, of subcontinental lithospheric mantle derivation and admixture of mantle plume (Youbi et al., 2020 and references therein). The second stage (590–550 Ma) was characterised by alkali-rich, OIB-like magmatism (Gumsley et al., 2020). The Tornquist Ocean had not yet opened, developing at ~550 Ma from a transform fault (Robert et al., 2021). At the same time, on the other side of Baltica (or the Balkatach continent; Zuza and Yin, 2017) the Paleoasian Ocean was forming (Gladkohub et al., 2013; Fig. 11). The remnants of this ocean are preserved as numerous ophiolites in Asia. The Palaeoasian Ocean that extended between Gondwana, Siberia and Baltica originated in Neoproterozoic (Zonenshain et al., 1990; Dobretsov et al., 2003; Kheraskova et al., 2010; Xu et al., 2013; Sengör et al., 2018).

The link to CIMP, which started to develop at ~615 Ma, seems to be the simplest explanation, however impossible, with the inventory of the co-existing exotic blocks and heavy minerals ages in the Magura Nappe, Outer Carpathians, showing the Variscan origin with inheritance of Cadomian basement (Bónová et al., 2018; Gawęda et al., 2019, 2021 and references therein). The documented rotation of the Outer Carpathians nappes during folding at ~60°C (Marton, 2020; Marton et al., 2015) could suggest a south-east origin of the exotic blocks. Moreover, the mafic Osielec suite show geochemical, isotopic and age similarity to suite I (the most widespread) of the Western Tatra amphibolites (see Gawęda et al., 2000 and Gawęda et al., 2017 for details; Figs. 8B). These amphibolites show also similar protolith age of ~600 Ma, similar Nd residential age (T_{DM}) at ~0.86–1.0 Ga and are interpreted in terms of Eastern Tornquist – Palaeoasian Ocean opening (Gawęda et al., 2017). The opening of the Palaeoasian Ocean at ~615 Ma on the southeast-east flank of Baltica/Balkatach was almost simultaneous with the formation of the Iapetus Ocean (Xu et al., 2013).

On the other hand, the geochemical features typical of subduction and continental arc formation (Figs. 9A, B) cannot be neglected. We interpret extension at the northern Gondwana margin initiated in a back-arc basin regime and consequently linked to the already opened Palaeoasian Ocean, breaking the continuity of the subduction zone (Fig. 11), what was observed in many other localities in the Neoproterozoic and interpreted as Neoproterozoic superplume activity (see Weber et al., 2020 for discussion). The Scythia microplate was further docked to Baltica (Kheraskova et al., 2015) and the original back-arc basin developed into the western part of Palaeoasian Ocean. The remnants of the Palaeoasian Ocean floor were probably obducted during late stages of Cadomian orogeny (e.g., Gawęda et al., 2019). They were incorporated in the Protocarpathian basement during Paleozoic times and elevated during Cretaceous–Paleogene, in the final stages of the Alpine orogenesis. The uplifted portions formed ridges dividing the Western Outer Carpathian basins (Golonka et al., 2019, 2021), underwent intensive erosion and were transported to the basins by gravity flows (Cieszkowski et al., 2017; Bónová et al., 2018; Gawęda et al., 2019 and references therein).

CONCLUSIONS

The mafic exotic blocks from the Osielec olistostrome represent the initial stage of Rodinia/Pannotia break-up and new ocean formation, with strong crustal contamination.

Apatite is a secondary phase, forming as a result of alteration and Ca mobilization. The U-Pb apatite cooling age of 613.92 ±1.57 Ma is almost identical (within age uncertainty) with previously published zircon U-Pb age, which implies fast cooling and simultaneous pervasive alteration with replacement of primary minerals by the new low-temperature assemblages and local shearing. The secondary mineral assemblage and temperature modelling allow to suppose the pervasive ocean-floor metamorphism.

The ~614 Ma mantle-related rocks can represent the Rodinia/Pannotia break-up event. Documented anticlockwise rotation of the Outer Carpathians and geochemical, isotopic and age similarity of the Osielec olistostrome fragments to some of the Western Tatra amphibolites suggest their eastern provenance and link to the Palaeoasian Ocean opening event.

Acknowledgements. We thank Ph.D. B. Marciniak-Maliszewska (Inter-Institutional Laboratory of Microanalyses of Minerals and Synthetic Substances, Warsaw) for her help during microprobe analyses, MSc. A. Zagórska (Institute of Geological Sciences at the Polish Academy of Sciences, Kraków, Poland) for her help with apatite separation, Prof. D. Chew (Trinity College Dublin, Ireland) for help during apatite dating, while Mrs. M. Horschinegg (Laboratory of Geochronology, Department of Lithospheric Research, University of Vienna) is acknowledged for the help in the Sr and Nd isotope whole-rock work. Dr. A. Gumsley is thanked for English correction. The comments of Dr I. Bubniak and two anonymous reviewers led to clearer presentation of the paper and are acknowledged. This study was supported by an internal project of INoZ UŚ, entitled “Neoproterozoic gabbroic-dioritic magmatism in the Protocarpathians” (AG, KS). This work is in tribute to Marek Cieszkowski.

REFERENCES

Anczkiewicz, R., Cieszkowski, M., Szczęch, M., Ślączka, A., Wolska, A., 2016. Ophiolite from Osielec – Magura Nappe, Outer Carpathians, Poland – a new approach to the problem. In: Environmental, Structural and Stratigraphical Evolution of the Western Carpathians n(ed. M. Šujan): 10th ESSE WECA Conference, 10th ESSEWECA Conference, December 1–2, 2016, Abstract Book: 9–10. Comenius University in Bratislava.

Bailey, S.W., 1980. Structures of layer silicates: in crystal structures of clay minerals and their X-ray identification. Mineralogical Society, London.

Bónová, K., Bóna, J., Kovačik, M., Mikuš, T., 2018. Heavy minerals and exotic pebbles from the Eocene flysch deposits of the Magura Nappe (Outer Western Carpathians, Eastern Slovakia): their composition and implications on the provenance. Turkish Journal of Earth Sciences, **27**: 64–88; https://doi.org/10.3906/yer-1707-9

Budzyń, B., Dunkley, D.J., Kusiak, M.A., Poprawa, P., Malata, T., Skiba, M., Paszkowski, M., 2011. SHRIMP U-Pb zircon chronology of the Polish Western Outer Carpatians source areas. Annales Societatis Geologorum Poloniae, **81**: 161–17.

Burda, J., Woskowicz-Ślęzak, B., Klötzli, U., Gawęda, A., 2019. Cadomian protolith ages of exotic mega blocks from Bugaj and Andrychów (Western Outer Carpathians, Poland) and their palaeogeographic significance. Geochronometria, **46**: 25–36; https://doi.org/10.1515/geochr-2015-0102

Cabanis, B., Lecolle, M., 1989. Le diagramme La/10–Y/15–Nb/8: Un outil pour la discrimination des series volcaniques et en evidence des mélange et la mise en evidence des processus de mélange et/ou de contamination crustale. Comptes Rendus de l'Académie des Sciences, **309**: 2023–2029.

Cannat, M., 1993. Emplacement of the mantle rocks in the sea floor at mid-ocean ridges. Journal of Geophysical Research, **98**: 4163–4172; https://doi.org/10.1029/92JB02221

Cathelineau, M., Nieva, D., 1985. A chlorite solid solution geothermometer. The Los Azufres (Mexico) geothermal system: Contribution to Mineralogy and Petrology, **91**: 235–244; https://doi.org/10.1007/BF00413350

Chew, D.M., Petrus, J.A., Kamber, B.S., 2014. U-Pb LA-ICPMS dating using accessory mineral standards with variable common Pb. Chemical Geology, **363**: 185–199; https://doi.org/10.1016/j.chemgeo.2013.11.006

Chew, D., Babechuk, M.G., Cogne, M., Mark, C., O'Sullivan, G.J., Henrichs, I.A., Doepke, D., McKenna, C.A., 2016. (LA,Q)-ICPMS trace element analyses of Durango and McClure Mountain apatite and implications for making natural LA-ICPMS mineral standard. Chemical Geology, **435**: 35–48; https://doi.org/10.1016/j.chemgeo.2016.03.028

Cieszkowski, M., Kysiak, T., Ślączka, A., Wolska, A., 2010. Olistoliths of gabbro from Osielec (Magura Nappe, Outer Carpathians, Poland). Mineralia Slovaka, **42**: 507–508; https://doi.org/10.7306/gq.1292

Cieszkowski, M., Golonka, J., Ślączka, A., Waśkowska, A., 2012. Role of the olistostromes and olistoliths in tectonostratigraphic evolution of the Silesian Basin in the Outer Carpathians. Tectonophysics, **568–569**: 248–265; https://doi.org/10.1016/j.tecto.2012.01.030

Cieszkowski, M., Kysiak, T., Szczęch, M., Wolska, A., 2017. Geology of the Magura Nappe in the Osielec area with emphasis on an Eocene olistostrome with metabasite olistoliths (Outer Carpathians, Poland). Annales Societatis Geologorum Poloniae, **87**: 169–182; https://doi.org/10.14241/asgp.2017.009

Cochrane, R., Spikings, R.A., Chew, D., Wotzlaw, J.-F., Chiaradia, M., Tyrrell, S., Schaltegger, U., Van der Lelijl, R., 2014. High temperature (>350°C) thermochronology and mechanisms of Pb loss in apatite. Geochimica et Cosmochimica Acta, **127**: 39–56; https://doi.org/10.1016/j.gca.2013.11.028

Costa, F., Dungan, M.A., Singer, B.S., 2002. Hornblende- and phlogopite-bearing gabbroic xenoliths from Volcán San Pedro (36°S), Chilean Andes: Evidence for melt and fluid migration and reactions in subduction-related plutons. Journal of Petrology, **43**: 219–241; https://doi.org/10.1093/petrology/43.2.219

Degen, T., Sadki, M., Bron, E., König, U., Nénert, G., 2014. The HighScore suite. Powder Diffraction, **29**(S2): S13–S18; https://doi.org/10.1017/S0885715614000840

Dewey, J.F., 1977. Suture zone complexities: a review. Tectonophysics, **40**: 53–67; https://doi.org/10.1016/0040-1951(77)90029-4

Dewey, J.F., 2005. Orogeny can be very short. Proceedings of the National Academy of Sciences USA, **102**: 15286–15293; https://doi.org/10.1073/pnas.0505516102

Dobretsov, N.L., Buslov, M.M., Vernikovsky, V.A. 2003. Neoproterozoic to Early Ordovician evolution of the Paleo-Asian Ocean: implications to the break-up of Rodinia. Gondwana Research, **6**: 143–15; https://doi.org/10.1016/S1342-937X(05)70966-7

Evans, B.W., Johannes, W., Otterdoom, H., Trommsdorff, V., 1976. Stability of chrysotile and antigorite in the serpentine multi-system. Schweizerische Mineralogische Petrographische Mitteilungen, **56**: 79–93.

Festa, A., Dilek, Y., Gawlick, H.-J., Missoni, S., 2014. Mass-transport deposits, olistostromes and soft sediment defromation in modern and ancient continental margins, and associated natural hazards. Marine Geology, **356**: 1–4; https://doi.org/10.1016/j.margeo.2014.09.001

Fitton, J.G., 2007. The OIB paradox. GSA Special Papers, **430**: 387–412; https://doi.org/10.1130/2007.2430(20)

Gawęda, A., Golonka, J., 2011. Variscan plate dynamics in the circum-Carpathian area. Geodinamica Acta, **24**: 141–155; https://doi.org/10.3166/ga.24.141-155

Gawęda, A., Winchester, J.A., Kozłowski, K., Narębski,W., Holland, G., 2000. Geochemistry and paleotectonic setting of the amphibolites from the Western Tatra Mountains. Geological Journal, **35**: 69–85; https://doi.org/10.1002/1099-1034(200004/06)35:2<69::AID-GJ838>3.0.CO;2-V

Gawęda, A., Burda, J., Golonka, J., Klötzli, U., Chew, D., Szopa, K., Wiedenbeck, M., 2017. The evolution of Eastern Tornquist-Paleoasian Ocean and subsequent continental collisions: a case study from the Western Tatra Mountains, Central Western Carpathians (Poland). Gondwana Research, **48**: 134–152; https://doi.org/10.1016/j.gr.2017.04.021

Gawęda, A., Golonka, J., Waśkowska, A., Szopa,, K., Chew, D., Starzec, K., Wieczorek, A., 2019. Neoproterozoic crystalline exotic clasts in the Polish Outer Carpathian flysch – remnants of the Proto-Carpathian continent? International Journal of Earth Sciences, **108**: 1409–1427; https://doi.org/10.1007/s00531-019-01713-x

Gawęda, A., Golonka, J., Chew, D., Waśkowska, A., Szopa, K., 2021. Central European Variscan basement in the Outer Carpathians: A case study from the Magura Nappe, Outer Western Carpathians, Poland. Minerals, 11: 256; https://doi.org/10.3390/min11030256

Gibson, I.L., Beslier, M.-O., Cornen, G., Milliken, K.L., Seifert, K.E., 1996. Major- and trace-element seawater alteration profiles in serpentinite formed during the development of the Iberia margin, site 8971. Proceedings of the Ocean Drilling Program, Scientific Results, **149**: 519–527; https://doi.org/10.2973/odp.proc.sr.149.219.1996

Gladkochub, D.P., Stanevich, A.M., Mazukabzov, A.M., Donskaya, T.V., Pisarevsky, S.A., Nicoll, G., Motova, Z.L., Kornolova, T.A., 2013. Early evolution of the Paleoasian Ocean: LA-ICP-MS dating of detrital zircon from Late Precambrian sequences of the southern margin of the Siberian craton. Russian Geology and Geophysics, **54**: 1150–1163; https://doi.org/10.1016/j.rgg.2013.09.002

Golonka, J., Gawęda, A., 2012. Plate Tectonic Evolution of the Southern Margin of Laurussia in the Paleozoic. In: Tectonics – Recent Advances (ed. E. Sharkov), ISBN 978-953-51-0675-3

In-Tech-Open: 261–282; https://doi.org/10.3166/ga.24.141-155

Golonka, J., Waśkowska, A., 2012. The Beloveža Formation of the Rača Unit in the Beskid Niski Mts. (Magura Nappe, Polish Flysch Carpathians) and adjacent parts of Slovakia and their equivalents in the western part of the Magura Nappe; remarks on the Beloveža Formation – Hieroglyphic Beds controversy. Geological Quarterly, **56**: 821–832; https://doi.org/10.7306/gq.1057

Golonka, J., Krobicki, M., Matyszkiewicz, J., Olszewska, B., Ślączka, A., Słomka, T., 2005. Geodynamics of ridges and development of carbonate platform within the Carpathian realm in Poland. Slovak Geological Magazine, **11**: 5–16.

Golonka, J., Waśkowska, A., Ślączka, A., 2019. The Western Outer Carpathians: Origin and evolution. Zeitschrift der Deutschen Gesellschaft für Geowissenschaften, **170**: 229–254; https://doi.org/10.1127/zdgg/2019/0193

Golonka, J., Gawęda, A., Waśkowska, A., 2021. Carpathians. In: Encyclopedia of Geology (eds. D. Alderton and S.A. Elias), 2nd edition vol. **4:** 372–381; https://doi.org/10.1016/B978-0-12-409548-9.12384-X

Gumsley, A., Manby, G., Domańska-Siuda, J., Nejbert, K., Michalski, K., 2020. Caught between two continents: first identification of the Ediacaran Central Iapetus Magmatic Province in Western Svalbard with palaeogeographic implications during final Rodinia breakup. Precambrian Research, **341**: 105622; https://doi.org/10.1016/j.precamres.2020.105622

Honnorez, J., 2003. Hydrothermal alteration vs. ocean-floor metamorphism. A comparison between two case histories: the TAG hydrothermal mound (Mid-Atlantic Ridge) vs. DSDP/ODP Hole 504B (Equatorial East Pacific). Comptes Rendus Geosciences, **335**: 781–824; https://doi.org/10.1016/j.crte.2003.08.009

Jowett, E., 1991. Fitting iron and magnesium into the hydrothermal chlorite geothermometer. In: Proceedings of the GAC/MAC/SEG Joint Annual Meeting, Toronto, Canada, May 27–29, 1991, **16**: A62.

Kheraskova, T.N., Bush, V.A., Didenko, A.N., Samygin, S.G., 2010. Breakup of Rodinia and early stages of evolution of the Paleoasian ocean. Geotectonics, **44**: 3–24; https://doi.org/10.1134/S0016852110010024

Kheraskova, T.N., Volozh Y.A., Antipov, M.P., Bykadorov, V.A., Sapozhnikov R.B., 2015. Correlation of Late Precambrian and Paleozoic events in the East European platform and the adjacent paleooceanic domains: Geotectonics, **49/1**: 27–52; https://doi.org/10.1134/S0016852115010021

Kováč, M., Plašienka, D., Soták, J., Vojtko, R., Oszczypko, N., Less, G., Králiková, S., 2016. Paleogene palaeogeography and basin evolution of the Western Carpathians, Northern Pannonian domain and adjoining areas. Global and Planetary Change, **140**: 9–27; https://doi.org/10.1016/j.gloplacha.2016.03.007

Kranidiotis, P., MacLean, W.H., 1987. Systematics of chlorite alteration at the Phelps Dodge massive sulfide deposit, Matagami, Quebec. Economic Geology, **82**: 1898–1911; https://doi.org/10.2113/gsecongeo.82.7.1898

Krestianinov, E., Amelin, Y., Neymark, L.A., Aleinikoff, J.N., 2021. U-Pb systematics of uranium-rich apatite from Adirondacks: inferences about regional geological and geochemical evolution, and evaluation of apatite reference materials for in situ dating. Chemical Geology, **20**: 120417; https://doi.org/10.1016/j.chemgeo.2021.120417

Książkiewicz, M., 1975. Bathymetry of the Carpathian flysch basin. Acta Geologica Polonica **25**: 309–368.

Książkiewicz, M., 1977. Hypothesis of plate tectonics and the origin of the Carpathians, Annales Societatis Geologorum Poloniae, **47**: 329–353.

Kysiak, T., 2010. Gabbro exotic rocks from the Rača Subunit of the Magura Nappe, West Outer Carpathians, Poland. In: 1st Students International Geological Conference, April 16–19, 2010, Kraków, Poland, p. 28.

Leake, B.E., Woolley, A.R., Arps, C.E.S., Birch, W.D., Gilbert, M.C., Grice, J.D., Hawthorn, F.C., Kao, A., Kisch, H.J., Krivovichev, V.G., Linthout, K., Laird, J., Mandarino, J.A., Maresch, W.V., Nickel, E.H., Rock, N.M.S., Schumacher, J.C., Smith, D.C., Stephenson, N.C.N., Ungaretti, L., Whittaker, E.J.W., Youzhi, G., 1998. Nomenclature of amphiboles: report of the subcommittee of amphiboles of the International Mineralogical Association, Commission on new minerals and mineral names. Canadian Mineralogist, **35**: 219–246.

Liew, T.C., Hofmann, A.W., 1988. Precambrian crustal components, plutonic associations, plate environment of the Hrcynian Fold Belt of Central Europe: Indications from a Nd and Sr isotopic study. Contributions to Mineralogy and Petrology, **98**: 129–138; https://doi.org/10.1007/BF00402106

Márton, E., 2020. Last scene in the large scale rotations of the Western Carpathians as reflected in paleomagnetic constraints. Geology, Geophysics and Environment, **46**: 109–133; https://doi.org/10.7494/geol.2020.46.2.109

Márton, E., Grabowski, J., Tokarski, A.K., Túnyi, I., 2015. Palaeomagnetic results from the fold and thrust belt of the Western Carpathians: an overview. Geological Society Special Publications, **425**: 7–36; https://doi.org/10.1144/SP425.1

McDonough, W.F., Sun, S.S., 1995. The composition of the Earth. Chemical Geology, **120**: 223–253; https://doi.org/10.1016/0009-2541(94)00140-4

Mével, C., 2003. Serpentinization of abyssal peridotites at mid-ocean ridges. Comptes Rendus Geosciences, **335**: 825–852; https://doi.org/10.1016/j.crte.2003.08.006

Moscardelli, L., Wood, L., 2007. New classification system for mass transport complexes in offshore Trinidad. Basin Research, **20**: 73–98; https://doi.org/10.1111/j.1365-2117.2007.00340.x

Murphy, J.B., Nance, R.D., Cawood, P.A., Collins, W.J., Dan, W., Doucet, L.S., Heron, P.J., Li, Z.-X., Mitchell, R.N., Pisarevsky, S., Pufahl, P.K., Quesada, C., Spencer, C.J., Strachan, R.A., Wu, L., 2021. Pannotia: in defence of its existence and geodynamic significance. Geological Society Special Publications, **503**: 13; https://doi.org/10.1144/SP503-2020-213

Ogata, K., Mutti, E., Pini, G.A., Tinterri, R., 2012. Mass transport-related stratal disruption within sedimentary mélanges: examples from the northern Apennines (Italy) and south-central Pyrenees (Spain). Tectonophysics, **568**: 185–199; https://doi.org/10.1016/j.tecto.2011.08.021

Oszczypko, N., 2010. Late Jurassic–Miocene evolution of the Outer Carpathian fold–and–thrust belt and its foredeep basin (Western Carpathians, Poland). Geological Quarterly, **50**: 169–194.

Paton, C., Hellstrom, J., Paul, B., Woodhead, J., Hergt, J., 2011. Iolite: freeware for the visualisation and processing of mass spectrometric data. Journal of Analytical Atomic Spectroscopy, **26**: 2508–2518; https://doi.org/10.1039/C1JA10172B

Paul, A.N., Spikings, R.A., Gaynor, S.P., 2021. U-Pb ID-TIMS reference ages and initial Pb isotope compositions for Durango and Wilberforce apatites. Chemical Geology, **586**: 120604; https://doi.org/10.1016/j.chemgeo.2021.120604

Pearce, J.A., 1982. Trace element characteristics of lavas from destructive plate boundaries. In: Andesites (ed. R.S. Thorpe): 525–547. Chichester, JohnWiley.

Pearce, J.A., 2008. Geochemical fingerprinting of oceanic basalts with applications to ophiolite classification and the search for Archean oceanic crust. Lithos, **100**: 14–48; https://doi.org/10.1016/j.lithos.2007.06.016

Pearce, J.A., Norry, M.J., 1979. Petrogenetic implications of Ti, Zr, Y and Nb variations in volcanic rocks. Contributions to Mineralogy and Petrology, **69**: 33–47; https://doi.org/10.1007/BF00375192

Pearce, J.A., Ernst, R.E., Peate, D.W., Rogers, C., 2021. LIP printing: Use of immobile element proxies to characterize Large Igneous Provinces in the geologic record. Lithos, **392–393**: 106068; https://doi.org/10.1016/j.lithos.2021.106068

Petrus, J.A., Kamber, B.S. 2012. VizualAge: a novel approach to laser ablation ICP-MS U-Pb geochronology data reduction. Geostandards and Geoananaltical Research, **36**: 247–270; https://doi.org/10.1111/j.1751-908X.2012.00158.x

Plašienka, D., Grecula, P., Putiš, M., Hovorka, D., Kovác, M., 1997. Evolution and structure of the Western Carpathians: an

overview. In: Geological evolution of the Western Carpathians (eds. P. Grecula, D. Hovorka, M. Putiš): 1–24. Mineralia Slovaca – Monograph Bratislava.

Poprawa, P., Malata, T., Pécskay, Z., Kusiak, M.A., Banaś, M., Paszkowski, M., 2006. Geochronology of the crystalline basement of the Western Outer Carpathians' source areas — constraints from the K/Ar dating of mica and Th–U–Pb chemical dating of monazite from the crystalline 'exotic' pebbles. Geolines **20**: 110–112.

Ridolfi, F., Renzulli, A., Puerini, M., 2010. Stability and chemical equilibrium of amphibole in calc-alkaline magmas: an overview, new thermobarometric formulations and application to subduction-related volcanoes. Contributions to Mineralogy and Petrology, **160**: 45–66; https://doi.org/10.1007/s00410-009-0465-7

Rioux, M., Jöns, N., Bowring, S., Lissenberg, C.J., Bach, W., Kylander-Clark, A., Hacker, B., Dudás, F., 2015. U-Pb dating of interspersed gabbroic magmatism and hydrothermal metamorphism during lower crustal accretion, Vema lithospheric section, Mid-Atlantic Ridge. Journal of Geophysical Research Solid Earth, **120**: 2093–2118; https://doi.org/10.1002/2014JB011668

Robert, B., Domeier, M., Jakob, J., 2021. On the origins of the Iapetus Ocean. Earth-Science Reviews, **221**: 103791; https://doi.org/10.1016/j.earscirev.2021.103791

Schmidt, S.M., Bernoulli, D., Fügenschuh, B., Matenco, L., Scheffer, S., Schuster, R., Tischler, M., Ustaszewski, K., 2008. The Alpine-Carpathian-Dinaridic orogenic system: correlation and evolution of tectonic units. Swiss Journal of Geosciences, **101**:139–183; https://doi.org/10.1007/ s00015-008- 1247-3

Schwarzenbarch, E.M., Steele-MacInnis, M., 2020. Fluids in submarine mid-ocean ridge hydrothermal setting. Elements, **16**: 389–394; https://doi.org/10.2138/gselements.16.6.389

Şengör, A.C., Natal'in, B.A., Sunal, G., van der Voo, R., 2018. The tectonics of the Altaids: Crustal growth during the construction of the continental lithosphere of Central Asia between ~750 and ~130 Ma ago. Annual Review of Earth and Planetary Sciences, **46**: 439–494; https://doi.org/10.1146/annurev-earth-060313-054826

Silantyev, S.A., Kostitsyn, Y.A., Cherkashin, D.V., Dick, H.J.B., Kelemen, P.B., Kononkova, N.N., Kornienko, E.M., 2008. Magmatic and metamorphic evolution of the oceanic crust in the western flank of the MAR crest zone at 15°44'N: Investigation of cores from sites 1275B and 1275D, JOIDES resolution Leg 209. Petrology, **16**: 353–375; https://doi.org/10.1134/S0869591108040036

Sinton, J.M., Detrick, R.S., 1992. Mid-ocean ridge magma chambers. Journal of Geophysical Research, **97**: 197–216; https://doi.org/10.1029/91JB02508

Stacey, J.S., Kramers, J.D., 1975. Approximation of terrestrial lead isotope evolution by a two stage model. Earth and Planetary Sci-ence Letters, **26**: 207–221; https://doi.org/10.1016/0012-821X(75)90088-6

Stampfli, G.M., Borel, G.D., Marchant, R., Mosar, J., 2002. Western Alps geological constraints on western Tethyan reconstructions. Journal of the Virtual Explorer, **8**: 77–106.

Steinmann, G., 1927. Die ophiolitischen Zonen in dem mediterraneen Kettengebirge. 14th International Geological Congress, Madrid Comptes Rendus, **2**: 638–667.

Szczuka, M., Gawęda, A., Waśkowska, A., Golonka, J., Szopa, K., Chew, D., Drakou, F., 2022. The Silesian Ridge in the light of petrological and LA-ICP-MS U-Pb analyses of cohesive debrites from the Istebna Formation (Silesian Nappe, Outer Western Carpathians, Poland). Geological Quarterly, **66**: 15–29; https://doi.org/10.7306/gq.1652

Szopa, K., Włodyka, R., Chew, D., 2014. LA-ICP-MS U-Pb apatite dating of Lower Cretaceous rocks from teschenite-picrite association in the Silesian Unit (southern Poland). Geologica Carpathica, **65**: 273–284; https://doi.org/10.2478/geoca-2014-0018

Ślączka, A., Kruglow, S., Golonka, J., Oszczypko, N., Popadyuk, I., 2006. The general geology of the Outer Carpathians, Poland, Slovakia, and Ukraine. AAPG Memoir, **84**: 221–258.

Unrug, R., 1968. The Silesian cordillera as the source of clastic material of the flysch sandstone of the Beskid Śląski and Beskid Wyspowy ranges (Polish Western Carpathians). Annales Societatis Geologorum Poloniae **38**: 155–164.

Vermeesh P., 2018. IsoplotR: A free and open toolbox for geochronology. Geoscience Frontiers, **9**: 1479–1493; https://doi.org/10.1016/j.gsf.2018.04.001

Weber, B., Schmitt, A.K., Cisneros de León, A., González-Guzman, R., Gerdes, A., 2020. Neoproterozoic extension and the Central Iapetus Magmatic Province in southern Mexico – New U-Pb ages, Hf-O isotopes and trace element data of zircon from the Chiapas Massif Complex. Gondwana Research, **88**: 1–20; https://doi.org/10.1016/j.gr.2020.06.022

Winkler, W., Ślączka, A., 1994. A late Cretaceous to Paleogene geodynamic model for the Western Carpathians in Poland. Geologica Carpathica, **45**: 71–82.

Wieser, T., 1952. The ophiolithe from Osielec (in Polish with English summary). Annales Societatis Geologorum Poloniae, **21**: 319–327.

Winchester, J.A., Floyd, P.A., 1977. Geochemical discrimination of different magma series and their differentition products using immobile elements. Chemical Geology, **20**: 325–343; https://doi.org/10.1016/0009-2541(77)90057-2

Xia, L., Li, X., 2019. Basalt geochemistry as a diagnostic indicator of tectonic setting. Gondwana Research, **65**: 43–97; https://doi.org/10.1016/j.gr.2018.08.006

Xu, B., Zou, H., Chen, Y., He, J., Wang, Y., 2013. The Sugetbrak basalts from northwestern Tarim Block of northwest China: Geochronology, geochemistry and implications for Rodinia breakup and ice age in the Late Neoproterozoic. Precambrian Research. **236**: 214–226; https://doi.org/10.1016/j.precamres.2013.07.009

Youbi, N., Ernst, R.E., Derlund, U.S., Boumehdi, M.A., Ait, Lahna, A., Tassinari, C.C.G., El Moume, W., Bensalah, M.K., 2020. The Central Iapetus magmatic province: an updated review and link with the ca. 580 Ma Gaskiers glaciation. GSA Special Papers, **544**: 35–66; https://doi.org/10.1130/2020.2544(02)

Zonenshain L.P., Kuzmin M.L., Natapov, L.N. 1990. Geology of the USSR: a plate-tectonic synthesis. Geodynamic Monograph, **21**: 1–242; https://doi.org/10.1029/GD021

Zuza, A.V., Yin, A., 2017. Balkatach hypothesis: A new model for the evolution of the Pacific, Tethyan, and Paleo-Asian oceanic domains. Geosphere, **13**: 1664–1712; https://doi.org/10.1130/GES01463.1

APPENDIX 1

Trace elements concentrations and selected petrological indices for the apatite from metagabbro from Osielec olistostrome

	Mn_m55	Sr_m88	Y_m89	La_m13	Ce_m14	Pr_m14	Nd_m14	Sm_m14	Eu_m15	Gd_m15	Tb_m159	Dy_m16	Ho_m16	Er_m16	Tm_m16	Yb_m17	Lu_m17	REE_{TOT}	Ce_N/Yb_N	Eu/Eu*	U	Th	Th/U
DB5_Ap_1	489	268.7	341.7	540	1344	152.2	655	116.6	14.3	99.4	11.65	66.1	12.72	33.83	4.38	26.6	3.851	**3080.63**	**13.27**	**0.40**	43.3	47.3	**1.09**
DB5_Ap_2	322.8	214.5	373.7	326.3	1115	148.6	693	132.9	15.59	113.6	13.38	75.4	14	37	4.75	28.18	4.177	**2721.88**	**10.39**	**0.39**	37.6	50.5	**1.34**
DB5_Ap_3	340.5	219	420.9	383.7	1296	167	772	146.1	17.49	125.7	14.77	84.1	15.59	40.5	5.31	31.5	4.7	**3104.46**	**10.81**	**0.39**	55.3	49.4	**0.89**
DB5_Ap_4	483.9	263.7	404.2	642	1626	187.8	817	138.8	17.18	117.2	14.06	78.7	15.05	41	5.12	31.23	4.506	**3735.65**	**13.67**	**0.41**	45.04	49.82	**1.11**
DB5_Ap_5	547.5	274.3	364.6	393	1174	145.7	661	123.7	14.71	104	12.56	72.2	13.68	36.19	4.74	27.65	4.05	**2787.18**	**11.15**	**0.40**	33.5	38.7	**1.16**
DB5_Ap_6	544.2	274.2	377.5	402.3	1272	159.7	707	129.2	15.15	108.5	13.18	73.9	14.13	37.62	4.79	27.86	4.137	**2969.47**	**11.99**	**0.39**	34.7	48	**1.38**
DB5_Ap_7	461.5	259.4	412.5	502	1507	179	788	143.3	16.77	120.6	14.49	82.1	15.52	40.78	5.31	32.02	4.65	**3451.54**	**12.36**	**0.39**	14.21	20.7	**1.46**
DB5_Ap_8	452.4	257.2	493	640	1585	179.6	791	150.7	16.43	133.1	16.44	94	18.48	48.8	6.33	37.78	5.55	**3723.21**	**11.02**	**0.35**	46.4	53.3	**1.15**
DB5_Ap_9	514.1	268.8	400.3	686	1626	185	831	154.5	14.57	140.6	15.58	84.8	15.34	38.06	4.56	26.88	3.912	**3826.8**	**15.89**	**0.30**	33.2	28.86	**0.87**
DB5_Ap_10	472.2	258.9	421	633	1583	186	851	165.7	14.11	149.4	16.88	92.3	16.84	41	4.88	27.97	3.98	**3786.06**	**14.86**	**0.27**	25.6	32.91	**1.29**
DB5_Ap_11	476.3	271.1	415	662	1618	186.4	854	163.7	13.95	152.9	17.12	92.5	16.66	41.06	4.84	28.1	3.99	**3855.22**	**15.12**	**0.27**	16.8	26.6	**1.58**
DB5_Ap_12	463.4	260.4	420.8	619.9	1584	185.3	853	162.7	14.72	150.7	17.19	92.6	16.73	41.5	4.78	27.87	3.96	**3774.95**	**14.93**	**0.29**	27.6	42.8	**1.55**
DB5_Ap_13	424.7	256.2	342.6	355.2	1123	141.4	661	115.1	15.46	97.6	11.59	66.7	12.62	33.8	4.46	26.21	3.905	**2668.05**	**11.25**	**0.44**	25.1	33.8	**1.35**
DB5_Ap_14	364.7	228.4	375	456.6	1331	157.9	690	124.2	17.23	107.8	12.78	73.7	14.06	37.9	4.91	30.12	4.51	**3062.71**	**11.61**	**0.45**	28.46	35.5	**1.25**
DB5_Ap_15	413	238.9	436	558	1605	190.8	826	146.4	18.32	120.6	14.73	83.8	16.09	44	5.93	36.6	5.42	**3671.69**	**11.52**	**0.42**	30.9	49.4	**1.60**
DB5_Ap_16	520.8	282.1	418	729	1702	184	786	139.1	17.53	120.7	14.13	81.6	15.27	41.3	5.36	32.8	4.81	**3873.6**	**13.63**	**0.41**	21.2	28.1	**1.33**
DB5_Ap_17	490.3	255.9	376.7	531.1	1370	158.9	698	130.3	14.6	112.3	13.54	76.5	14.76	38.06	4.79	27.58	4.179	**3194.61**	**13.05**	**0.37**	47.2	51.3	**1.09**
DB5_Ap_18	358	222.9	423.9	211.3	813	118.3	602.7	121.5	14.82	109.4	13.35	77.3	14.91	41.58	5.7	35.9	5.72	**2185.48**	**5.95**	**0.39**	48.3	26.3	**0.54**
DB5_Ap_19	548.5	272.2	382.6	772	1777	193.2	807	134.5	17.44	110.9	13.04	74.2	14.16	38.17	4.99	30.56	4.377	**3991.54**	**15.27**	**0.44**	22.8	38.9	**1.71**
DB5_Ap_20	504.1	267.2	362.4	687	1617	177.8	731	125.2	15.43	103.9	12.27	70.7	13.21	35.56	4.491	27.45	4.074	**3625.09**	**15.47**	**0.41**	23.9	32.6	**1.36**
DB5_Ap_21	431.5	235.6	466	368	1162	152.5	711	138.8	16.67	124.6	15.35	90	17.16	46.1	6.1	36.7	5.26	**2890.24**	**8.32**	**0.39**	29.2	39.2	**1.34**
DB5_Ap_22	521	254.4	399.2	403	1213	153.6	721	135.2	15.06	121.5	14.21	79.9	15.22	38.6	4.86	27.63	4.015	**2946.8**	**11.53**	**0.36**	32.6	41.8	**1.28**
DB5_Ap_23	383.8	244.9	469	440.1	1389	174.4	791	148.9	19.97	126.6	15.19	88.7	17.31	46.9	6.07	37.6	5.66	**3307.4**	**9.70**	**0.44**	46.5	61.6	**1.32**
DB5_Ap_24	327.1	226.1	331.8	227.6	769	100.7	475	94.6	13.55	84.6	10.58	62.7	12.03	33.52	4.41	27.39	4.149	**1919.83**	**7.37**	**0.46**	30.1	37	**1.23**
DB5_Ap_25	343	228.9	415	365	1163	149.1	696	135.4	16.19	117.5	14.26	82.3	15.44	41.8	5.45	32.3	4.85	**2838.59**	**9.46**	**0.39**	18.6	29.2	**1.57**
DB5_Ap_26	512.6	282	507	887	2059	228.6	954	167.3	21.33	140.1	17.08	98.6	18.38	50.8	6.6	41.88	6.03	**4696.7**	**12.91**	**0.42**	41.2	69.1	**1.68**
DB5_Ap_27	515.8	282	529.2	910	2139	240.1	1019	176.7	24.05	147.4	17.81	103.3	19.41	52.5	6.82	42.47	6.26	**4904.82**	**13.23**	**0.45**	59.6	81.1	**1.36**
DB5_Ap_28	358.1	243.5	322.4	342.4	933	114.7	558	107.9	12.59	98.6	11.4	65.6	12.29	32.6	4	24.01	3.79	**2320.88**	**10.21**	**0.37**	49.8	22.69	**0.46**
DB5_Ap_29	491	258.8	424.4	511	1393	167.5	759	145	17.56	128.6	15.13	85.4	15.88	42.1	5.52	33.5	4.99	**3324.18**	**10.92**	**0.39**	49.6	47.8	**0.96**
DB5_Ap_30	462.8	264.6	404.4	546	1413	163.8	724	130.4	16.45	111.3	13.6	79	14.96	40.04	5.31	32.17	4.73	**3294.76**	**11.54**	**0.42**	22	28.7	**1.30**

DB5_Ap_31	552	276.4	462.2	807	1920	213.9	895	157	20.32	131.3	15.57	91.1	17.15	46.78	6.06	36.23	5.32	**4362.73**	**13.92**	**0.43**	19.1	30.8	**1.61**
DB5_Ap_32	538.9	301.5	467.7	710	1692	190.3	817	145.1	17.79	125.4	15.43	89	17.3	46.41	6.22	37.5	5.51	**3914.96**	**11.85**	**0.40**	6.31	11.44	**1.81**
DB5_Ap_33	435	255.5	371	421	1143	136.6	615	118.2	17.3	101.2	12.25	70.3	13.46	37.1	4.87	29.2	4.51	**2723.99**	**10.28**	**0.48**	64.9	49.9	**0.77**
DB5_Ap_34	419.2	242	437	388.1	1213	157.9	737	142.4	17.8	122	14.88	84	16.52	44.62	5.71	34.51	5.22	**2983.66**	**9.23**	**0.41**	59.8	59.6	**1.00**
DB5_Ap_35	438.8	243.3	432	427.8	1241	156	712	138.2	15.69	121.8	14.76	85.7	16.16	43.9	5.67	32.8	4.81	**3016.29**	**9.94**	**0.37**	54.9	66.9	**1.22**
DB5_Ap_36	472.3	256.5	438.6	628	1617	185.9	807	144.2	19.4	124.5	15.12	86.6	16.35	44.82	5.86	35.88	5.2	**3735.83**	**11.84**	**0.44**	61.9	73.7	**1.19**
DB5_Ap_37	450.8	264.6	352.9	502.1	1277	147.5	645	116.2	15.83	97.1	11.92	69.1	12.89	34.86	4.59	28.39	4.2	**2966.68**	**11.81**	**0.45**	46.7	50.6	**1.08**
DB5_Ap_38	579.7	285.2	381.1	753	1717	184.4	778	134.6	16.93	111.5	13.52	76	14.28	38.24	4.86	29.35	4.198	**3875.88**	**15.36**	**0.42**	31.6	47.7	**1.51**
DB5_Ap_39	463	260.9	472.3	531	1613	197	896	159.4	18.42	138	16.3	92.9	17.32	46.96	6.06	36.95	5.35	**3774.66**	**11.47**	**0.38**	49.6	56.5	**1.14**
DB5_Ap_40	495	258.1	440.3	570	1540	184	804	146.9	17.68	126.3	14.96	86	16.44	43.89	5.68	35.43	5.36	**3596.64**	**11.42**	**0.40**	43.8	62.7	**1.43**
DB5_Ap_41	527.9	281.3	439.5	786	1862	204.9	874	150.2	18.65	125	15.06	85.9	16.29	44.36	5.96	35.9	5.31	**4229.53**	**13.62**	**0.41**	18.43	23.9	**1.30**
DB5_Ap_42	486.8	265.4	420.4	659	1617	186.7	803	142	18.53	119.9	14.56	84.1	15.83	42.8	5.56	34.75	5.09	**3748.82**	**12.22**	**0.43**	38.6	54	**1.40**
DB5_Ap_43	446.2	244.9	437.2	624	1609	188.8	826	148.4	19.98	123.1	15.07	86.1	16.18	43.28	5.64	34.38	5.32	**3745.25**	**12.29**	**0.45**	71.8	68.9	**0.96**
DB5_Ap_44	384.8	234.3	327.1	236.1	695	92.7	462.5	97.8	15.14	88.9	10.83	63.8	12.12	33.64	4.216	26.62	4.343	**1843.71**	**6.86**	**0.49**	65.8	21.95	**0.33**
DB5_Ap_45	529.2	256	341.6	433.8	1209	143.5	641.2	114.6	14.94	95.1	11.51	65.1	12.73	33.85	4.233	25.18	3.72	**2808.46**	**12.61**	**0.44**	58.9	35	**0.59**
DB5_Ap_46	579.8	283.8	483	852	2012	223.2	951	167	20.54	144.8	17.27	99.7	18.7	49.5	6.32	37.49	5.5	**4605.02**	**14.10**	**0.40**	27.25	41.89	**1.54**
DB5_Ap_47	464.4	251	408	475	1281	157.1	702	130.6	16.36	110.5	13.39	78.9	14.95	40.24	5.25	31.02	4.77	**3061.08**	**10.85**	**0.42**	63.4	40.04	**0.63**
DB5_Ap_48	522.1	281.3	426	863	1976	214.7	908	157.9	17.75	133.7	15.12	85.1	15.92	41.7	5.42	33.33	4.76	**4472.4**	**15.57**	**0.37**	22.8	28.9	**1.27**
DB5_Ap_49	420.6	260.8	384.3	580.9	1495	174.4	758	133.6	15.87	114.2	13.64	76.8	14.37	38.9	4.95	30.13	4.376	**3455.14**	**13.03**	**0.39**	14.14	22.2	**1.57**
DB5_Ap_50	441.5	249.4	479.8	572.6	1547	183.8	820	151.1	18.47	130	16.01	93	17.44	47.49	6.28	38.84	5.8	**3647.83**	**10.46**	**0.40**	33.26	46.4	**1.40**
DB5_Ap_51	434.8	230	382	355	1125	143.2	658	125	13.96	111.6	13.31	76.3	14.37	38.2	4.91	29.1	4.296	**2712.25**	**10.15**	**0.36**	21.6	33.7	**1.56**
DB5_Ap_52	500.4	285.9	431.7	804	1869	207.9	868	150.3	19.87	121.1	14.68	84.7	15.96	42.46	5.66	34.17	4.99	**4242.79**	**14.37**	**0.45**	28.3	44.3	**1.57**
DB5_Ap_53	332.1	222.6	503.5	264.6	952	131.8	655	133.3	19.69	117.2	15.1	90.8	17.9	51.39	7.26	47.85	7.69	**2511.58**	**5.23**	**0.48**	74.7	35	**0.47**
DB5_Ap_54	308.2	237.2	287.6	421	1224	144.1	613.4	105.7	11.68	86	10.39	58.4	10.86	29.47	3.686	21.86	3.326	**2743.87**	**14.71**	**0.37**	18.11	39	**2.15**
DB5_Ap_55	498.8	282.9	475.5	556.4	1579	199.2	926	176.8	15.22	151.9	17.48	97.6	18.16	46.28	5.63	32.23	4.568	**3826.47**	**12.87**	**0.28**	12.73	18.87	**1.48**
DB5_Ap_56	484.7	280.2	363.8	686	1650	179.7	741	125.4	16.41	104.3	12.34	71.7	13.66	37.09	4.9	29.88	4.381	**3676.76**	**14.50**	**0.44**	31.65	49.5	**1.56**
DB5_Ap_59	338.2	226.4	354.7	304	1000	129.1	608	116.8	13.51	101.8	12.4	70.2	13.35	35.22	4.64	27.35	3.967	**2440.34**	**9.60**	**0.38**	16.21	26.6	**1.64**
DB5_Ap_60	397.1	240.7	439.7	532	1532	181.2	792	141.2	18.91	121.3	14.8	87	16.09	44.68	5.89	36.11	5.41	**3528.59**	**11.14**	**0.44**	37.9	51.7	**1.36**
DB5_Ap_61	**609**	319.9	474	1240	2650	280	1116	184	23.2	145.8	17.08	96.1	17.58	46.2	6.19	36.61	5.39	**5864.15**	**19.01**	**0.43**	18	32.1	**1.78**
DB5_Ap_62	551.8	284	437	892	2013	216.1	886	153.3	18.85	127.5	15.41	88.5	16.66	43.7	5.62	34	4.98	**4515.62**	**15.55**	**0.41**	36	47.3	**1.31**
DB5_Ap_63	567.2	287.1	423	893	1973	211.1	859	148.9	17.79	124.4	14.94	85.3	15.8	42.6	5.48	33.6	4.88	**4429.79**	**15.42**	**0.40**	22	31.3	**1.42**
DB5_Ap_64	392.1	233	390.2	395.4	1310	164.9	746	131.5	14.13	108.3	13.1	74.7	14.17	38.46	4.8	28.82	4.194	**3048.47**	**11.94**	**0.36**	38.6	58.9	**1.53**
DB5_Ap_65	434.6	251.5	319.9	396	1116	135.9	608	113.9	15.88	97.4	11.57	64.1	12.08	31.53	3.93	22.55	3.39	**2632.23**	**13.00**	**0.46**	53.2	23.9	**0.45**

DB5_Ap_66	515.1	279	332.6	659	1558	169.3	709	122.9	16.1	101	11.93	67.6	12.71	32.4	4.218	24.75	3.58	**3492.49**	**16.53**	**0.44**	48.5	48.4	**1.00**
DB5_Ap_67	495.9	253.7	478	580	1561	185.6	819	150.7	16.77	129.3	16.18	92.8	17.64	47.5	5.96	36.9	5.21	**3664.56**	**11.11**	**0.37**	43.9	58.9	**1.34**
DB5_Ap_68	470.6	267.1	404.2	756	1757	194.3	811	136.6	20.04	114.4	13.56	78.8	14.65	40.35	5.31	34.02	5.19	**3981.22**	**13.56**	**0.49**	49.3	62.5	**1.27**
DB5_Ap_69	477.8	257.9	378.6	564.6	1500	168.7	708	122.1	17.72	102.9	12.26	72.4	13.81	37.97	5.101	31.34	4.707	**3361.61**	**12.57**	**0.48**	32.2	42.8	**1.33**
DB5_Ap_70	461.7	252.9	377.5	558	1493	172.4	744	130.8	16.84	108.5	12.84	72.75	13.89	37.71	4.936	30.02	4.49	**3400.18**	**13.06**	**0.43**	67.6	48.02	**0.71**
DB5_Ap_71	539.2	296.4	496.6	806	1882	209.4	933	178.1	15.94	169	19.35	108.1	19.7	48.54	5.729	32.73	4.615	**4432.2**	**15.10**	**0.28**	16.65	22.5	**1.35**
DB5_Ap_72	370	238.1	418.7	365.9	1244	159.7	740	140.4	15.11	122.7	14.53	84.3	15.83	42.07	5.36	31.39	4.37	**2985.66**	**10.41**	**0.35**	6.36	9.64	**1.52**
DB5_Ap_73	504	263.8	407	760	1802	196	831	146.7	17.17	124.3	14.48	83.4	15.62	41	5.28	31.5	4.64	**4073.09**	**15.02**	**0.39**	43.3	56.2	**1.30**
DB5_Ap_74	482.6	268.9	351.7	519	1388	159.6	716	122.6	16.06	102	12.08	68.55	12.98	34.7	4.459	27.07	3.938	**3187.04**	**13.47**	**0.44**	43.8	37.9	**0.87**
DB5_Ap_75	367.6	228.4	387.3	389	1223	151.9	705	131.8	14.91	115.5	13.59	78.2	14.59	38.47	4.86	28.25	4.225	**2913.3**	**11.37**	**0.37**	35.5	50.7	**1.43**
DB5_Ap_76	417.8	252.6	315.1	442.6	1240	146.5	639.9	114.8	13.76	95.3	11.38	63.5	11.73	31.31	3.995	22.7	3.468	**2840.94**	**14.35**	**0.40**	51.3	39.3	**0.77**
DB5_Ap_77	425.5	249.6	326.7	377	1086	129.9	579	107.5	14.5	91.2	10.91	62.8	12.03	32.31	4.3	25.52	3.846	**2536.82**	**11.18**	**0.45**	24.1	35.3	**1.46**
DB5_Ap_78	568.4	268.2	516.5	771	1944	221.5	951	170.8	21.94	143.3	17.87	102.2	19.07	51.75	6.69	40.1	5.82	**4467.04**	**12.73**	**0.43**	55	67	**1.22**
DB5_Ap_79	473.4	260.3	325.8	547.6	1367	153.4	663	116.9	14.79	100.1	11.86	67.6	12.61	33.2	4.16	24.51	3.63	**3120.36**	**14.65**	**0.42**	28.2	39.9	**1.41**
DB5_Ap_80	555.3	282.8	408.8	792	1814	196.1	807	140.2	18.59	115.1	13.76	78.1	14.74	40.7	5.314	32.15	4.72	**4072.47**	**14.82**	**0.45**	36.4	43.7	**1.20**
DB5_Ap_81	524.2	273	393.3	725	1726	184.7	787	135.5	17.61	111.8	13.33	76.1	14.54	39.59	5.13	31.8	4.626	**3872.73**	**14.26**	**0.44**	27.9	40	**1.43**
DB5_Ap_82	395.5	232.7	397	336	1025	128.7	607	118.8	17	105.5	13.02	74.9	14.47	40.2	5.21	32.4	5.13	**2523.33**	**8.31**	**0.46**	79	41.4	**0.52**
DB5_Ap_83	369.9	232.1	429.9	299.6	952	125	603	119.9	15.61	110.3	13.66	82	15.67	42.69	5.58	35.52	5.75	**2426.28**	**7.04**	**0.41**	72.3	30.6	**0.42**
DB5_Ap_84	474.8	252.6	401	418	1184	142.6	631	119.3	17.89	101	12.77	74.9	14.13	39.7	5.3	33.7	5.12	**2799.41**	**9.23**	**0.50**	40.1	55.6	**1.39**
DB5_Ap_85	371.3	219.8	499.7	420.8	1305	164.1	755	148.3	19.53	129.6	16.18	94	18.16	50.31	6.59	41.8	6.23	**3175.6**	**8.20**	**0.43**	84.6	51.2	**0.61**
DB5_Ap_86	538.9	259.6	421	556	1468	171.5	747	137.2	19.81	117.1	14.23	81.4	15.31	41	5.32	32.1	4.79	**3410.76**	**12.01**	**0.48**	70.9	61.5	**0.87**
DB5_Ap_87	530.7	259.2	511.7	798	1938	217.5	926	164.3	23.15	136.8	16.72	96.9	18.74	51	6.79	42.4	6.37	**4442.67**	**12.00**	**0.47**	64.8	78.6	**1.21**
DB5_Ap_88	471.1	249.1	405.7	562	1488	172.6	765	137	17.94	119.5	14.2	82.2	15.56	42.03	5.46	32.31	4.66	**3458.46**	**12.10**	**0.43**	60.8	52.1	**0.86**
DB5_Ap_89	369.7	216.9	456	200.3	766	109.3	558	122.6	21.15	114.6	14.77	87.2	16.98	47.3	5.97	36.9	5.38	**2106.45**	**5.45**	**0.54**	15.45	17.5	**1.13**
DB5_Ap_90	499.3	279.4	397.2	723	1841	209.5	887	146.8	16.94	115.2	13.85	78.1	14.41	39.93	5.06	31.11	4.489	**4126.39**	**15.54**	**0.40**	29.26	46.5	**1.59**
DB5_Ap_91	508	275.4	358.5	614	1447	158.7	676	113.6	15.67	96.8	11.81	68.4	12.93	35.2	4.5	28.27	4.08	**3286.96**	**13.44**	**0.46**	38.3	47.6	**1.24**
DB5_Ap_92	527.2	291.7	399.4	797	1826	195.3	819	140.6	17.03	115.2	13.77	78.4	14.88	40.35	5.34	32.12	4.739	**4099.73**	**14.93**	**0.41**	22.6	27.2	**1.20**
DB5_Ap_93	508.9	280.7	417.9	820	1874	204	850	143.9	17.92	124.1	14.13	81.9	15.26	41.47	5.3	32.65	4.8	**4229.43**	**15.07**	**0.41**	33.56	40.2	**1.20**
DB5_Ap_94	404.2	238.1	436.4	410.8	1221	150.5	700	136.3	18.67	120	14.83	85.2	16.48	43.54	5.64	34.7	5.31	**2962.97**	**9.24**	**0.44**	83	53.6	**0.65**
DB5_Ap_95	464	270.5	359.9	638	1576	175.7	736	129.6	15.17	107.8	13.14	74.2	13.71	36.03	4.54	26.64	3.806	**3550.34**	**15.54**	**0.39**	46.1	46	**1.00**
DB5_Ap_96	361.6	250.5	481	529.2	1577	188	837	157.8	19.16	133.2	16.12	93.6	17.5	48.31	6.2	38.68	5.63	**3667.4**	**10.71**	**0.40**	7.61	21.3	**2.80**
DB5_Ap_97	527.3	257.4	361.3	569	1425	158.7	681	118.5	15.62	101.2	12.11	69.9	13.38	37.03	4.79	30.09	4.91	**3241.23**	**12.44**	**0.43**	55.9	42.7	**0.76**
DB5_Ap_98	410.5	235.8	393	504	1443	169.6	756	133.6	17.19	112	13.43	77.4	14.59	39.3	5.12	30.7	4.57	**3320.5**	**12.35**	**0.43**	59.8	59.6	**1.00**

DB5_Ap_99	529.1	281.5	376.8	748	1753	190.8	798	132.6	17.66	108.3	12.93	74.7	13.86	37.89	4.83	30.19	4.34	**3927.1**	**15.25**	**0.45**	35.3	50.6	**1.43**
DB5_Ap_100	431.6	242.9	320.7	365	1116	136.2	623	113.2	14.36	97.8	11.36	65.9	12.22	32.23	4.08	24.94	3.55	**2619.84**	**11.75**	**0.42**	52.1	38.3	**0.74**
DB5_Ap_101	520.4	284	515	977	2235	237.6	980	172	20.52	142.6	17.57	100.2	19.07	51.3	6.94	42.55	6.16	**5008.51**	**13.80**	**0.40**	27.4	37.6	**1.37**
DB5_Ap_102	433.6	257.1	394.7	588	1554	177.8	776	137.1	15.38	115.3	13.99	79.6	14.9	40.28	5.078	29.7	4.47	**3551.6**	**13.74**	**0.37**	22.1	27.3	**1.24**
DB5_Ap_103	497.4	277.9	446.2	846	2063	226.6	966	166.5	17.12	137.5	15.91	88.2	16.48	43.18	5.46	32.84	4.71	**4629.5**	**16.50**	**0.34**	31.8	43.5	**1.37**
DB5_Ap_104	507.1	274.7	417.6	872.8	2034	218.4	896	149.5	18.61	124	14.79	84.8	15.8	41.93	5.34	32.25	4.699	**4512.92**	**16.56**	**0.42**	23.2	47.8	**2.06**

APPENDIX 2

LA-ICP-MS U-Pb isotopic data of apatites from the Osielec gabbro (D5 sample), Osielec olistostrome, Outer Western Carpathians, Poland

sample No	$^{207}Pb/^{235}U$	2s	$^{206}Pb/^{238}U$	2s	r	$^{238}U/^{206}Pb$	2s	$^{207}Pb/^{206}Pb$	2s	r	$^{206}Pb/^{238}U$ age	2s	$^{207}Pb/^{235}U$ age	2s	$^{207}Pb/^{206}Pb$ age	2s	^{207}Pb corr	2s
DB5_Ap_1	2.67	0.091	0.12	0.003	0.3385	8.6580	0.22	0.1690	0.0043	0.2369	704.6	18.3	1320.7	45.0	2547.8	64.8	615.3	16.0
DB5_Ap_2	2.72	0.085	0.11	0.003	0.2907	8.8339	0.22	0.1763	0.0041	0.2194	691.3	17.1	1332.6	41.7	2618.4	60.9	597.2	14.8
DB5_Ap_3	2.09	0.078	0.11	0.003	0.2089	9.0827	0.24	0.1373	0.0043	0.2003	673.3	17.7	1145.9	42.7	2193.4	68.7	612.8	16.1
DB5_Ap_4	2.58	0.11	0.11	0.003	0.4222	8.8889	0.23	0.1656	0.0056	-0.0002	687.3	17.7	1293.8	55.2	2513.7	85.0	602.4	15.8
DB5_Ap_5	3.32	0.1	0.12	0.003	0.3373	8.4890	0.25	0.1996	0.0053	0.3918	717.9	20.7	1485.5	44.8	2822.9	75.0	600.7	17.5
DB5_Ap_6	3.12	0.1	0.12	0.003	0.2247	8.6806	0.23	0.1959	0.0051	0.3367	702.9	18.3	1438.1	46.1	2792.3	72.7	590.8	15.6
DB5_Ap_7	5.68	0.22	0.14	0.004	0.5144	7.0872	0.22	0.2918	0.0081	0.2093	850.9	26.5	1928.3	74.7	3427.2	95.1	621.5	20.8
DB5_Ap_8	2.56	0.16	0.11	0.003	0.6838	8.8028	0.26	0.1632	0.0076	-0.4408	693.6	20.8	1289.3	80.6	2489.1	115.9	610.2	18.9
DB5_Ap_9	3.56	0.13	0.12	0.003	0.1878	8.0257	0.21	0.2081	0.0065	0.3290	757.0	20.0	1540.7	56.3	2890.8	90.3	627.0	17.3
DB5_Ap_10	4.27	0.17	0.13	0.003	0.6190	7.7340	0.20	0.2390	0.0065	-0.1544	783.9	20.0	1687.6	67.2	3113.3	84.7	620.8	16.7
DB5_Ap_11	6.48	0.44	0.15	0.005	0.8071	6.8074	0.24	0.3120	0.013	-0.4925	883.6	31.3	2043.2	138.7	3530.8	147.1	624.8	25.8
DB5_Ap_12	3.94	0.11	0.13	0.003	0.3707	7.9302	0.21	0.2270	0.0042	0.4020	765.6	20.0	1621.1	45.3	3031.0	56.1	616.8	16.3
DB5_Ap_13	4.15	0.15	0.13	0.003	0.2238	7.9365	0.21	0.2399	0.007	0.4187	765.0	20.0	1664.2	60.2	3119.3	91.0	604.3	16.8
DB5_Ap_14	3.27	0.13	0.12	0.003	0.4062	8.4602	0.24	0.1987	0.006	0.0701	720.2	20.7	1473.9	58.6	2815.5	85.0	603.5	17.7
DB5_Ap_15	3.14	0.15	0.12	0.003	0.5700	8.4459	0.23	0.1939	0.0066	-0.2053	721.3	19.5	1442.6	68.9	2775.5	94.5	608.7	17.1
DB5_Ap_16	5.57	0.19	0.14	0.004	0.4726	7.0175	0.20	0.2849	0.0079	0.1486	858.8	24.1	1911.5	65.2	3390.0	94.0	635.0	19.3
DB5_Ap_17	2.62	0.091	0.12	0.003	0.3873	8.6059	0.21	0.1661	0.0041	0.1247	708.7	17.7	1307.1	45.3	2518.7	62.2	621.5	15.5
DB5_Ap_18	2.04	0.069	0.11	0.003	0.5648	9.2851	0.22	0.1376	0.0033	-0.1442	659.4	15.9	1130.0	38.2	2197.2	52.7	599.5	14.3
DB5_Ap_19	5.15	0.19	0.14	0.003	0.2799	7.3529	0.18	0.2738	0.0084	0.1248	822.0	20.6	1844.4	68.0	3327.9	102.1	617.5	17.3
DB5_Ap_20	4.71	0.22	0.13	0.004	0.4269	7.5415	0.20	0.2540	0.0088	-0.0077	802.7	21.8	1769.0	82.6	3209.9	111.2	621.7	18.6
DB5_Ap_21	3.77	0.21	0.12	0.003	0.5019	8.0841	0.22	0.2182	0.0089	-0.1341	751.8	20.7	1586.4	88.4	2967.5	121.0	613.3	18.3
DB5_Ap_22	3.05	0.11	0.12	0.003	0.5216	8.6730	0.24	0.1939	0.0057	-0.0264	703.5	19.5	1419.0	51.3	2775.5	81.6	593.0	16.8
DB5_Ap_23	2.41	0.14	0.11	0.003	0.6046	8.8106	0.23	0.1549	0.0073	-0.3396	693.0	17.7	1245.6	72.4	2400.7	113.1	616.7	16.5
DB5_Ap_24	3.02	0.12	0.12	0.003	0.3833	8.4317	0.22	0.1860	0.0052	0.2210	722.5	18.9	1413.2	56.1	2707.1	75.7	616.7	16.4
DB5_Ap_25	4.09	0.17	0.13	0.004	0.4301	7.9051	0.22	0.2335	0.0073	0.0758	767.9	21.2	1652.3	68.7	3076.2	96.2	612.7	17.9
DB5_Ap_26	3.05	0.15	0.12	0.003	0.6582	8.0972	0.22	0.1764	0.0054	-0.3322	750.7	20.7	1420.2	69.8	2619.3	80.2	650.4	18.1
DB5_Ap_27	2.72	0.27	0.12	0.004	0.9677	8.6281	0.30	0.1631	0.0098	-0.8227	706.9	24.4	1333.9	132.4	2488.1	149.5	622.4	22.5
DB5_Ap_28	2.35	0.073	0.11	0.003	0.1239	8.8496	0.22	0.1500	0.004	0.4769	690.1	17.1	1227.6	38.1	2345.9	62.6	618.1	15.3
DB5_Ap_29	2.39	0.075	0.12	0.003	0.3515	8.5397	0.22	0.1489	0.0035	0.2543	713.9	18.3	1238.1	38.9	2333.3	54.8	641.0	16.3
DB5_Ap_30	4.27	0.26	0.13	0.004	0.6570	7.6687	0.25	0.2360	0.01	-0.3405	790.1	26.1	1687.6	102.8	3093.2	131.1	628.9	22.4

DB5_Ap_31	5.06	0.28	0.14	0.005	0.6619	7.2411	0.24	0.2680	0.011	-0.3575	833.9	27.2	1829.4	101.2	3294.4	135.2	632.9	23.0
DB5_Ap_32	14.03	0.6	0.21	0.008	0.6204	4.7870	0.18	0.4920	0.02	0.2648	1223.0	45.1	2751.7	117.7	4217.4	171.4	605.8	38.2
DB5_Ap_33	2.07	0.072	0.11	0.003	0.3082	8.8183	0.23	0.1333	0.0039	0.2950	692.5	17.7	1139.9	39.6	2141.9	62.7	634.1	16.1
DB5_Ap_34	1.96	0.064	0.11	0.003	0.0097	9.3633	0.22	0.1344	0.0038	0.3936	654.1	15.3	1101.5	36.0	2156.2	61.0	597.1	13.9
DB5_Ap_35	2.46	0.1	0.11	0.003	0.4176	8.7108	0.21	0.1544	0.0047	-0.0734	700.6	17.1	1261.2	51.2	2395.2	72.9	624.0	15.3
DB5_Ap_36	2.43	0.14	0.12	0.003	0.8207	8.5837	0.25	0.1513	0.0068	-0.6020	710.4	20.7	1251.5	72.1	2360.7	106.1	635.7	19.0
DB5_Ap_37	2.55	0.11	0.11	0.003	0.3895	8.7184	0.23	0.1621	0.0053	0.0951	700.0	18.3	1287.3	55.5	2477.7	81.0	617.0	16.3
DB5_Ap_38	3.84	0.14	0.12	0.003	0.3722	8.0064	0.21	0.2222	0.0061	0.2086	758.7	19.4	1601.2	58.4	2996.7	82.3	615.5	16.4
DB5_Ap_39	1.92	0.065	0.10	0.003	0.4043	9.5694	0.23	0.1346	0.0035	0.0921	640.7	15.3	1087.7	36.8	2158.8	56.1	584.4	13.9
DB5_Ap_40	2.43	0.075	0.11	0.003	0.4648	8.9445	0.23	0.1584	0.004	0.1648	683.2	17.7	1252.7	38.6	2438.7	61.6	604.7	15.6
DB5_Ap_41	5.33	0.19	0.14	0.004	0.0658	7.1942	0.18	0.2791	0.0092	0.4170	839.0	21.1	1873.7	66.8	3357.9	110.7	625.5	18.1
DB5_Ap_42	2.97	0.094	0.12	0.003	0.4712	8.5543	0.22	0.1820	0.004	0.2185	712.7	18.3	1399.7	44.3	2671.2	58.7	611.4	15.7
DB5_Ap_43	1.90	0.061	0.11	0.003	0.4406	9.3371	0.24	0.1282	0.003	0.0544	655.9	16.5	1080.4	34.7	2073.4	48.5	603.6	15.0
DB5_Ap_44	2.02	0.072	0.11	0.003	0.3122	8.9847	0.23	0.1304	0.0039	0.1960	680.3	17.1	1120.9	40.0	2103.4	62.9	625.0	15.6
DB5_Ap_45	2.29	0.074	0.11	0.003	0.1157	8.8810	0.21	0.1497	0.0039	0.3868	687.8	16.5	1210.1	39.1	2342.5	61.0	616.2	14.8
DB5_Ap_46	4.13	0.13	0.13	0.003	0.1037	7.8989	0.21	0.2399	0.0067	0.4429	768.4	20.0	1659.9	52.3	3119.3	87.1	607.1	16.7
DB5_Ap_47	2.20	0.067	0.12	0.003	0.1279	8.6881	0.21	0.1392	0.0035	0.3896	702.3	17.1	1180.4	36.0	2217.3	55.8	638.4	15.4
DB5_Ap_48	4.85	0.17	0.13	0.004	0.4300	7.5131	0.21	0.2634	0.0071	0.2223	805.5	22.4	1793.6	62.9	3267.2	88.1	614.7	18.1
DB5_Ap_49	5.61	0.21	0.14	0.004	0.6251	7.2780	0.22	0.2949	0.0089	-0.0748	829.9	25.4	1917.6	71.8	3443.6	103.9	602.1	20.2
DB5_Ap_50	3.04	0.12	0.12	0.003	0.4930	8.6430	0.22	0.1877	0.0062	0.0186	705.8	18.3	1417.7	56.0	2722.1	89.9	600.4	16.1
DB5_Ap_51	4.14	0.17	0.13	0.004	0.5756	7.5472	0.20	0.2274	0.0069	-0.0316	802.1	21.2	1662.2	68.3	3033.8	92.1	647.3	18.0
DB5_Ap_52	3.73	0.15	0.12	0.003	0.5675	8.1433	0.23	0.2238	0.0065	-0.0206	746.7	20.7	1577.8	63.5	3008.2	87.4	603.8	17.4
DB5_Ap_53	1.71	0.058	0.11	0.003	0.2456	9.3023	0.23	0.1129	0.0031	0.2807	658.2	16.5	1011.5	34.3	1846.6	50.7	617.9	15.3
DB5_Ap_54	3.76	0.15	0.12	0.004	0.0569	8.0064	0.22	0.2197	0.0081	0.4000	758.7	21.3	1584.2	63.2	2978.5	109.8	617.8	18.5
DB5_Ap_55	7.27	0.29	0.15	0.004	0.6278	6.5062	0.19	0.3420	0.011	-0.0100	921.7	26.4	2145.1	85.6	3671.7	118.1	619.1	21.5
DB5_Ap_56	3.31	0.11	0.12	0.003	0.1342	8.1235	0.21	0.1958	0.0052	0.4789	748.4	19.5	1483.2	49.3	2791.5	74.1	630.8	16.7
DB5_Ap_57	4.71	0.18	0.13	0.004	0.2796	7.7700	0.21	0.2620	0.0082	0.2788	780.4	21.2	1769.0	67.6	3258.8	102.0	595.9	17.7
DB5_Ap_58	2.72	0.16	0.12	0.003	0.3972	8.5763	0.23	0.1704	0.0085	-0.0758	711.0	18.9	1333.9	78.5	2561.6	127.8	619.9	17.6
DB5_Ap_59	7.38	0.3	0.16	0.005	0.5024	6.3980	0.19	0.3388	0.0095	0.0189	936.2	27.6	2158.5	87.7	3657.4	102.6	633.4	21.4
DB5_Ap_60	3.56	0.12	0.12	0.003	0.2833	8.0386	0.20	0.2080	0.0057	0.2769	755.8	18.8	1541.3	51.9	2890.0	79.2	626.1	16.1
DB5_Ap_61	5.76	0.36	0.14	0.004	0.6433	6.9979	0.22	0.2920	0.014	-0.3055	861.0	26.5	1940.4	121.3	3428.3	164.4	629.2	24.0
DB5_Ap_62	2.53	0.077	0.11	0.003	0.3646	8.8496	0.23	0.1623	0.0036	0.3575	690.1	17.7	1279.5	39.0	2479.8	55.0	607.8	15.5
DB5_Ap_63	2.32	0.076	0.11	0.003	0.1542	8.9847	0.23	0.1496	0.0042	0.3391	680.3	17.7	1218.1	39.9	2341.4	65.7	609.3	15.8

DB5_Ap_64	2.80	0.13	0.12	0.003	0.6744	8.5985	0.21	0.1746	0.0058	-0.3608	709.2	17.7	1355.5	62.9	2602.2	86.4	614.7	15.7
DB5_Ap_65	2.75	0.13	0.12	0.003	0.3772	8.5251	0.22	0.1704	0.0067	0.0328	715.0	18.3	1342.1	63.4	2561.6	100.7	623.5	16.6
DB5_Ap_66	2.63	0.096	0.12	0.003	0.3736	8.5911	0.22	0.1639	0.0045	0.2118	709.8	18.3	1309.6	47.8	2496.3	68.5	624.4	16.1
DB5_Ap_67	3.83	0.15	0.12	0.003	0.4433	8.0192	0.21	0.2224	0.0068	-0.0081	757.6	19.4	1599.1	62.6	2998.1	91.7	614.3	16.6
DB5_Ap_68	2.15	0.066	0.11	0.003	0.4296	9.0009	0.22	0.1398	0.0029	0.1477	679.1	16.5	1163.8	35.8	2224.7	46.1	616.2	14.8
DB5_Ap_69	6.09	0.25	0.15	0.005	0.4371	6.6845	0.21	0.2963	0.0091	0.2104	898.7	27.6	1988.8	81.6	3451.0	106.0	653.8	22.1
DB5_Ap_70	11.20	0.46	0.19	0.006	0.0001	5.2966	0.16	0.4290	0.018	0.5729	1114.9	34.2	2539.9	104.3	4014.0	168.4	637.6	31.7
DB5_Ap_71	2.96	0.092	0.12	0.003	0.4747	8.2781	0.23	0.1777	0.0038	0.3839	735.2	20.7	1398.4	43.4	2631.5	56.3	635.3	17.7
DB5_Ap_72	2.78	0.096	0.11	0.003	0.4911	8.7489	0.21	0.1757	0.0043	-0.0178	697.7	17.1	1349.9	46.6	2612.7	63.9	603.4	14.9
DB5_Ap_73	2.78	0.099	0.12	0.003	0.3982	8.6957	0.22	0.1751	0.0047	0.1247	701.7	17.7	1351.3	48.1	2607.0	70.0	607.5	15.5
DB5_Ap_74	2.30	0.087	0.11	0.003	0.2662	8.7413	0.22	0.1460	0.0044	0.2929	698.3	17.7	1213.2	45.8	2299.6	69.3	628.9	16.0
DB5_Ap_75	4.06	0.13	0.12	0.003	0.1956	8.0321	0.21	0.2328	0.0061	0.3365	756.4	19.4	1646.3	52.7	3071.4	80.5	603.7	16.2
DB5_Ap_76	2.64	0.094	0.12	0.003	0.4021	8.4104	0.23	0.1610	0.0041	0.2068	724.2	19.5	1312.1	46.7	2466.2	62.8	640.1	17.1
DB5_Ap_77	3.74	0.16	0.12	0.003	0.3287	8.0257	0.20	0.2171	0.0084	0.1623	757.0	18.8	1580.0	67.6	2959.3	114.5	618.7	16.9
DB5_Ap_78	3.74	0.13	0.13	0.003	0.4399	7.8740	0.21	0.2125	0.0058	0.1364	770.7	20.6	1580.0	54.9	2924.7	79.8	634.8	17.4
DB5_Ap_79	3.99	0.13	0.13	0.003	0.5292	7.8125	0.19	0.2252	0.0046	-0.0284	776.4	18.8	1631.6	53.2	3018.2	61.7	627.7	15.5
DB5_Ap_80	1.92	0.081	0.11	0.003	0.5855	8.9366	0.22	0.1241	0.0036	-0.3009	683.8	17.1	1087.7	45.9	2016.0	58.5	633.5	15.7
DB5_Ap_81	1.81	0.055	0.11	0.003	0.0001	9.4073	0.23	0.1241	0.0033	0.5580	651.2	15.9	1048.7	31.9	2016.0	53.6	602.4	14.6
DB5_Ap_82	2.87	0.12	0.12	0.003	0.3402	8.4317	0.22	0.1745	0.0057	0.1716	722.5	18.9	1374.1	57.5	2601.3	85.0	626.7	16.7
DB5_Ap_83	1.49	0.047	0.10	0.003	0.2100	9.6339	0.23	0.1054	0.0022	0.2169	636.6	15.3	927.9	29.2	1721.3	35.9	602.9	14.2
DB5_Ap_84	2.22	0.077	0.11	0.003	0.4128	8.8731	0.20	0.1414	0.0032	-0.0277	688.4	15.9	1188.6	41.2	2244.4	50.8	623.6	14.3
DB5_Ap_85	2.24	0.083	0.11	0.003	0.5452	8.7796	0.23	0.1420	0.0034	-0.0099	695.4	18.3	1193.3	44.2	2251.7	53.9	629.6	16.4
DB5_Ap_86	2.28	0.078	0.11	0.003	0.1730	8.8810	0.22	0.1463	0.004	0.2764	687.8	17.1	1206.4	41.3	2303.1	63.0	619.0	15.4
DB5_Ap_87	4.98	0.21	0.14	0.004	0.2989	7.3529	0.19	0.2641	0.0088	0.1385	822.0	21.2	1815.9	76.6	3271.3	109.0	627.3	18.1
DB5_Ap_88	3.73	0.1	0.12	0.003	0.1249	8.0710	0.20	0.2213	0.0049	0.4772	753.0	18.8	1578.7	42.3	2990.2	66.2	611.4	15.6
DB5_Ap_89	3.31	0.16	0.12	0.004	0.4762	8.1433	0.26	0.1964	0.0079	-0.0942	746.7	23.7	1483.4	71.7	2796.5	112.5	628.7	20.7
DB5_Ap_90	5.12	0.25	0.13	0.004	0.7773	7.5019	0.23	0.2826	0.0086	-0.3865	806.7	24.2	1839.4	89.8	3377.4	102.8	596.5	19.5
DB5_Ap_91	3.36	0.14	0.12	0.003	0.4210	8.3822	0.22	0.2047	0.0062	0.0103	726.5	19.5	1495.1	62.3	2864.0	86.7	603.7	16.7
DB5_Ap_92	1.76	0.069	0.11	0.003	0.4669	9.1241	0.23	0.1151	0.0034	-0.0278	670.4	17.1	1031.6	40.4	1881.5	55.6	628.0	15.8
DB5_Ap_93	2.67	0.088	0.11	0.003	0.3675	8.8810	0.22	0.1704	0.0039	0.1513	687.8	17.1	1321.3	43.5	2561.6	58.6	599.0	14.9
DB5_Ap_94	8.86	0.59	0.16	0.007	0.6248	6.1387	0.27	0.3830	0.021	-0.1759	972.9	42.4	2323.7	154.7	3843.6	210.7	605.9	36.1
DB5_Ap_95	2.30	0.078	0.12	0.003	0.0440	8.6430	0.23	0.1446	0.0043	0.4132	705.8	18.9	1211.7	41.1	2283.0	67.9	637.1	17.0
DB5_Ap_96	2.14	0.1	0.11	0.003	0.4890	8.9206	0.23	0.1380	0.0049	-0.1674	684.9	17.7	1162.5	54.3	2202.3	78.2	623.1	16.2

DB5_Ap_97	3.62	0.11	0.13	0.003	0.3737	7.9239	0.21	0.2084	0.0043	0.2420	766.2	20.0	1554.8	47.2	2893.1	59.7	634.7	16.7
DB5_Ap_98	2.35	0.082	0.11	0.003	0.5059	9.0909	0.23	0.1559	0.0039	-0.0221	672.7	17.1	1226.6	42.9	2411.7	60.3	597.2	15.2
DB5_Ap_99	4.66	0.23	0.13	0.004	0.7690	7.5075	0.23	0.2513	0.0075	-0.3484	806.1	24.8	1760.1	86.9	3193.0	95.3	627.1	20.2
DB5_Ap_100	4.75	0.19	0.13	0.004	0.5654	7.5586	0.21	0.2599	0.007	0.0017	801.0	22.4	1776.1	71.0	3246.1	87.4	614.5	18.2
DB5_Ap_101	3.53	0.15	0.12	0.003	0.1609	8.1766	0.19	0.2094	0.0078	0.1147	743.8	17.6	1534.0	65.2	2900.9	108.1	614.4	15.9
DB5_Ap_102	4.98	0.2	0.14	0.004	0.5411	7.3475	0.19	0.2648	0.0076	-0.1028	822.6	21.8	1815.9	72.9	3275.5	94.0	627.0	17.9